



HAL
open science

High-Resolution Observations and Tracking of a Dual-Core Anticyclonic Eddy in the Algerian Basin

P. Garreau, F. Dumas, S. Louazel, A. Stegner, B. Le Vu

► **To cite this version:**

P. Garreau, F. Dumas, S. Louazel, A. Stegner, B. Le Vu. High-Resolution Observations and Tracking of a Dual-Core Anticyclonic Eddy in the Algerian Basin. *Journal of Geophysical Research. Oceans*, 2018, 123 (12), pp.9320-9339. 10.1029/2017JC013667 . hal-02411309

HAL Id: hal-02411309

<https://hal.science/hal-02411309>

Submitted on 14 Dec 2019

HAL is a multi-disciplinary open access archive for the deposit and dissemination of scientific research documents, whether they are published or not. The documents may come from teaching and research institutions in France or abroad, or from public or private research centers.

L'archive ouverte pluridisciplinaire **HAL**, est destinée au dépôt et à la diffusion de documents scientifiques de niveau recherche, publiés ou non, émanant des établissements d'enseignement et de recherche français ou étrangers, des laboratoires publics ou privés.

1
2
3
4
5
6
7
8
9
10
11
12
13
14
15
16
17
18
19
20
21
22
23
24

High-resolution observations and tracking of a dual-core anticyclonic eddy in the Algerian Basin

P. Garreau¹, F. Dumas², S. Louazel², A. Stegner³, B. Le Vu³

¹ IFREMER, Univ. Brest, CNRS UMR 6523, IRD, Laboratoire d'Océanographie Physique et Spatiale (LOPS), IUEM, 29280, Plouzané, France

² SHOM, Service Hydrographique et Océanographique de la Marine, 13 rue de Chatellier, CS592803, 29228 Brest CEDEX2, France

³ Laboratoire de Météorologie Dynamique (LMD), CNRS UMR 8539, Ecole Polytechnique, 91128 Palaiseau, France

Corresponding author: Pierre Garreau (pierre.garreau@ifremer.fr)

Key Points:

- An Algerian eddy was tracked for 8 months in the Mediterranean Sea revealing interactions and mass exchanges between individual structures.
- The dual-core eddy was composed of a surface water mass (Atlantic Water) and a modal water mass (Western Intermediate Water).
- High-resolution sampling revealed submesoscale structures.

25 Abstract

26

27 Mesoscale dynamics in the Mediterranean Sea have been investigated for years and anticyclonic
28 eddies are regularly observed features in the Algerian Basin. Here, we used the AMEDA eddy
29 detection algorithm to track and monitor a particular anticyclonic eddy from its birth to its death.
30 The analysis of remote-sensing datasets (AVISO and SST) revealed that this anticyclone split
31 from an Algerian eddy in October 2015, interacted with the North Balearic Front and merged
32 seven months later, in May 2016, with a similar Algerian eddy. In early spring 2016, a field
33 experiment during the ProtevsMed 2016 cruise thoroughly investigated this eddy, when it was
34 located near the North Balearic Front, taking high-resolution (Seasoar) hydrological transects,
35 several CTD casts and LADCP measurements. In addition, four drifting buoys were released in
36 the eddy core. These in situ measurements revealed that the vertical structure of this anticyclone
37 was made of two water lenses of very different origins (Atlantic Water above and Western
38 Intermediate Water below) spinning together. In the vicinity of the North Balearic Front, which
39 may act as a dynamical barrier to such oceanic structures, the eddy interacted with a subsurface
40 anticyclonic eddy made of modal water, which fostered cross-front exchanges generating
41 filaments by stirring. The high-resolution sampling revealed fine-scale structures both adjacent to
42 the eddy and within its core

43

44

45 **1 Introduction**

46

47 Eddies are oceanic structures, transporting and trapping water masses and biochemical
48 properties, shielding their core from strong mixing with the surrounding environment.
49 Conversely, when mesoscale dynamics are intense, interactions between structures foster at
50 small-scale exchanges between water masses at their periphery (Robinson, 1983). A major
51 oceanographic challenge is to understand the role played by mesoscale eddies in the distribution
52 of temperature, salinity and biological productivity in the ocean and how they participate in the
53 vertical exchange between the ocean interior and the surface layer (McWilliams, 2013;
54 McGillicuddy, 2016). In the Algerian Basin, anticyclonic eddies spread Atlantic Water (AW)
55 northwards, feed the West Corsica Current and provide potential energy to the cyclonic
56 circulation in the northern part of the western Mediterranean Basin (Millot, 1999).

57

58 Described nearly 30 years ago by Millot et al. (1990) using infrared sea surface temperature
59 (SST) images, Algerian Eddies (AEs) are generated by the unstable meanders of the Algerian
60 Current (Taupier-Letage et al. 2003; Salas et al. 2003; Font et al., 2004).. A large number of AEs
61 detach from the Algerian coast upstream of the Sardinian Channel (8°E) and then move in a
62 counterclockwise manner northwestwards up to the North Balearic Front (NBF), the Balearic
63 Islands, reaching even the Almeria-Oran Front (Perez, 2003). A deep cyclonic circulation within
64 the Algerian Basin has been demonstrated using RAFOS drifters and two subsurface gyres were
65 identified, centered at around 37°30'N-2°30'E and 38°30'N-6°00'E (Testor et al., 2005).

66 Revisiting 20 years of altimetric data with several eddy detection algorithms, Escudier et al.
67 (2016a) confirmed the two counterclockwise circulations of the eddies in the Algerian Basin and
68 identified two preferential areas of detachment from the Algerian Current within the intervals of
69 2°E – 4°E and 6°E – 8°E . The dynamics of the Algerian Basin are dominated by numerous
70 anticyclonic eddies, filaments and meandering. Despite intense interactions between these
71 structures leading to merging, squeezing or squashing processes, individual eddies can be
72 followed for a few months and sometimes for a few years (Puillat et al., 2002). Although they
73 may extend over a wide part of the water column (up to 1000 m), the eddies intensify in the first
74 300-400 m, near the surface. The maximal azimuthal velocity of such anticyclones is about 0.4-
75 0.6 m/s (Ruiz et al., 2002)

76

77 The anticyclonic eddies of the Algerian Basin are mainly composed of AW coming from the
78 Algerian Current, which is a major source of eddy formation. Nevertheless, other identified
79 water masses of the Mediterranean Sea are involved and redistributed by these mesoscale
80 structures. Previous hydrographic surveys (Benzohra & Millot 1995a, 1995b; Fuda et al., 2000)
81 revealed relatively unmixed Western Intermediate Water (WIW; formerly called Winter
82 Intermediate Water) and Levantine Intermediate Water (LIW) associated with AEs. Benzohra et
83 al. (1995a) discussing the origin of the WIW found under the core of a large open-sea eddy of
84 120-140 km in diameter just after its detachment. He suggested that the WIW is formed locally
85 in winter by AW cooling or advected from its formation areas in the northern part of the basin.
86 After winter, some lenses of the WIW may survive for months as modal waters called “wedgies”
87 — winter intermediate eddies — in the Balearic Basin (Pinot & Ganachaud, 1999; Juza et al.,
88 2013). This water mass is characterized by a subsurface minimum of temperature between the
89 AW and the LIW, deflecting the later to a deeper zone. These isolated water masses may also
90 persist, as smaller structures, called Submesoscale Coherent Vortices (SCVs) (Bosse et al., 2016).
91 They are able to move to the Algerian Basin. The exact process that associate secondary water
92 masses (WIW, LIW) with the AEs has not yet been clearly identified.

93

94 The mesoscale patterns of eddies has been extensively observed, but the non-linear dynamics and
95 the interactions with the atmosphere generating finer scale motions have mainly been explored
96 only numerically and theoretically. Recent high resolution numerical modelling of eddies have
97 described submesoscale processes (Brannigan, 2016; Brannigan et al. 2017; Zhong et al. 2017).
98 Likewise, observed eddies appear often more complex than expected. Although satellites
99 imagery reveals spiraling in eddy cores as a surface signature of ageostrophic dynamics, the
100 complete observation of the 3-D dynamics and associated tracer fields are incomplete. Obtained
101 during the OMEGA-2 field experiment in November 1996 (Allen et al., 2008), high-resolution
102 observations of a weddy in the Algerian Basin, near the Almeria-Oran frontal area, show an
103 oblate lens of 20 km radius, 150 m thick, centered at 250 m depth, caused anticyclonic
104 circulation near the front, with associated currents on the order of 0.20 m/s. However, no clear
105 connection with a surface signature of an associated AE was demonstrated. A few years later, a

106 more obvious patch of WIW was described in the same area and the effect of this WIW core on
107 vertical turbulence was explored (Forryan et al., 2012). Combining gliders and remote sensing,
108 Ruiz et al. (2009) investigated a 100 km wide AE in the eastern Alboran Sea. They captured
109 fine-scale structures, sub-ducting to 120 m depth, on its edge and assessed the structure and the
110 order of magnitude of the vertical velocity. Further to the east, Cotroneo et al. (2016) studied a
111 60 km wide AE near 4°W-38°N and described submesoscale features mainly using chlorophyll
112 and dissolved oxygen tracers. Although the lack of horizontal resolution prevents a thorough
113 interpretation of the results, the effects on biochemistry tracers suggested the occurrence of some
114 submesoscale processes. Despite these recent developments in glider technology, synoptic
115 observations of “secondary” circulation in the eddy core or periphery remains under-sampled and
116 more thorough high-resolution surveys of mesoscale eddies are sorely needed.

117
118 The Protevs-Med 2016 cruise aimed to describe and understand the origin of the freshwater
119 involved in the North Current and the associated large cyclonic circulation in the northwestern
120 Mediterranean Sea, sometimes called Northern Gyre. In this context, AW bodies close to the
121 NBF were of primary interest. Applying a very high-resolution survey, we expected to find fine-
122 scale structures in the NBF. Serendipitously, a very singular anticyclonic eddy was present near
123 the front, providing a unique opportunity to observe submesoscale structures revealing secondary
124 circulations, vertical motion in the core, intense stirring in the periphery and strong interaction
125 with adjacent dynamical structures. This is the first dual-core eddy to be described in the western
126 Mediterranean Sea. It was tracked from its birth by eddy splitting until its death by merging, and
127 intensively surveyed during a field experiment (Section 2). Eddy tracking revealed that eddy-
128 eddy interactions play a role in north-south mass exchanges (Section 3). The high-resolution in
129 situ observations highlight small-scale processes embedded in mesoscale eddy dynamics; the
130 interaction of the eddy with NBF is described (Section 4). An interpretation of the process
131 leading to this dual-core body is discussed (Section 5). Finally, we summarize our results in a
132 conclusion (Section 6).

133

134

135 **2 Materials and Methods**

136

137 **2.1 Eddy detection and tracking using remote-sensing products**

138

139 To investigate the temporal behavior of the mesoscale eddies in the Algerian Basin, we used the
140 geostrophic velocity fields, produced by Salto/Duacs, distributed by AVISO, and derived from
141 absolute dynamical topography (ADT). The “all-sat-merged” series combines, for the years
142 1993-2016, up-to-date datasets with up to four satellites at a given time (Pujol et al., 2016), using
143 all missions available at a given time (Topex/Poseidon, ERS-1 and -2, Jason-1 and -2, Saral,
144 Cryosat-2 and Envisat missions). This specific product for the Mediterranean Sea is projected on
145 a 1/8° Mercator grid with time intervals of 24 h. The horizontal resolution of the gridded velocity
146 fields ($dX \approx 12$ km), based on track frames, along-track filtering and optimal interpolation, can

147 hardly resolve the internal deformation radius R_d , which is approximately 8–15 km in the
148 western Mediterranean Sea (Escudier et al., 2016b). The surface signature of large mesoscale
149 eddies with a characteristic radius that exceed the deformation radius can generally be detected
150 (Isern-Fontanet et al., 2006; Pascual et al., 2007; Rio et al., 2007; Amitai et al., 2010; Mkhinini
151 et al., 2014; Ioannou et al., 2017). Nevertheless, the spatio-temporal heterogeneity of the
152 altimetric tracks of satellites may also miss eddies or induce systematic bias on eddy intensity.

153

154 To follow the complete trajectory of the surveyed anticyclone and its interaction with
155 neighboring eddies, we used the AMEDA algorithm (Le Vu et al., 2018). This automatic eddy
156 detection and tracking algorithm uses a hybrid methodology based on dynamical physical
157 parameters (local normalized angular momentum) and geometrical properties of the velocity
158 field (closed streamlines). It quantifies the dynamical characteristics of the detected eddies and
159 especially the mean velocity profile. When the distance to the center increases, the mean
160 azimuthal velocity increases until a maximum value (V_{max}) is reached. A *characteristic*
161 *contour*, i.e. the closed streamline corresponding to the maximum azimuthal velocity, is obtained
162 for each eddy. A typical eddy radius R_{max} , also called the *speed radius* in previous studies
163 (Chelton et al., 2011), is then computed from the area $A = \pi R_{max}^2$ surrounded by the characteristic
164 contour. However, most importantly, the tracking procedure identifies merging and splitting
165 events. Therefore, it can better track the origin of the water masses inside the detected eddy.

166

167 2.2 In situ sampling strategy

168

169 Given that the eddy was detected in mid-March, before the field experiment (Figures 2 e-f) south
170 of the NBF, it was targeted from 27 March to 1 April 2016 taking advantage of a
171 meteorologically favorable period. It was sampled with

- 172 • a towed undulating vehicle, the SeaSoar designed and built by Chelsea Instruments;
173 mounted on either side were two Sea-Bird SBE-9 (with SBE 3 temperature and SBE 4
174 conductivity sensors) instruments and a chlorophyll *a* WetStar WET Labs fluorometer;
- 175 • CTD casts performed with the Sea-Bird SBE-9 instrument and a LADCP (Lowered
176 Acoustic Doppler Profiler, RDI 150 kHz) mounted in a General Oceanics 12-place
177 rosette frame fitted with 12 Niskin bottles;
- 178 • drifters with holey sock positioned at 50 m, below the expected Ekman layer. After
179 removing spikes, raw positions were resampled hourly using a B-spline interpolation,
180 keeping the inertial oscillations.

181

182 Unfortunately the hull mounted ADCPs were out of order. Salinity was measured using the practical
183 salinity scale. The towed undulating SeaSoar platform was operated with a horizontal velocity
184 ranging from 8 to 9 knots. At this speed, the vehicle can descend to 400 m depth, allowing quasi-
185 synoptic sampling of the eddy with a horizontal resolution of about 1 nautical mile. The duration
186 of a typical transect of 150km took half a day, which is less than the inertial period. The

187 sampling strategy is summarized in Figure 1. The first SeaSoar zonal transect (GT1) crossed the
188 eddy center estimated at 4°40' E 39°50' N. The second transect (GT2, not shown) is a transit
189 transect outside the eddy up to its northern boundary. The GT3 transect is a meridional transect
190 sampling the eddy from its northern edge, near the North Balearic Front, to the eddy center.
191 Unfortunately, the vessel was not allowed to extend further south (unauthorized area). The last
192 transect (GT5, not shown) crossed the eddy center again from the southwest to the northeast and
193 confirmed the position of the eddy center and some cylindrical symmetry of the eddy pattern. On
194 29 March, nine CTD casts (numbered CTD013 to CTD021 from eddy center towards the NBF)
195 with LADCP profiles were taken along the GT3 transect to obtain additional information on
196 deeper layers (at least down to 1500m). In the early morning, four drifters (with holey socks
197 immersed at 50 m depth) were dropped successively near the estimated eddy center during the
198 transit between CTD0013 and CDT0014. Lastly, four parallel meridional SeaSoar transects
199 (RDT1 to RDT4) were performed along the northern edge to investigate the interactions with the
200 NBF and the possible presence of fine-scale structures. A typical profile of the northern area was
201 then sampled by a final CTD cast (CDT022) and LADCP measurements before leaving the area
202 at the very end of the meteorologically favorable period. The total duration of this in situ
203 sampling was about four days but the drifters remained trapped in the eddy core for
204 approximately one month.

205

206 **3 Eddy detection and tracking**

207

208 **3.1 The past trajectory of the anticyclone: from its birth to the North Balearic Front**

209

210 The use of the automatic eddy detection and tracking algorithm AMEDA made it possible to
211 trace the anticyclonic eddy back in time. Besides we also used high-resolution SST images
212 (VIIRS/Suomi-NPP) and the trajectories of the few surface drifters located in the area to validate
213 the eddy trajectory. The combination of these different datasets and the characteristic eddy
214 contours computed using AMEDA are shown in Figure 2. We found that the surveyed
215 anticyclone arose from the splitting of an AE that occurred in late October 2015. On 2 October
216 2015 (Figure 2a, b) the AMEDA algorithm clearly identified a large-scale anticyclone centered
217 on 38.5°N 5.7°E, associated with a 25 cm ADT dome. At that time, one surface drifter (red
218 trajectory in Figure 2a) looped around the characteristic contours of the eddy, i.e. the streamline
219 corresponding to the maximum of the mean azimuthal velocity (thick blue contour in Figure 2a,
220 b). From this specific drifter trajectory, we estimated the eddy velocity V_{\max} to be 30–35 cm/s
221 and its characteristic radius R_{\max} to be 50 km. These in situ measurements are in good agreement
222 with the analysis of the AVISO geostrophic velocity field given by the AMEDA algorithm,
223 which estimated a mean radius of R_{\max} of 50 km and a maximal azimuthal velocity V_{\max} of 32
224 cm/s for the first week of October 2015. The small Rossby number ($Ro = V_{\max}/(f R_{\max})$; ~ 0.07)
225 corresponds to a large mesoscale eddy satisfying the geostrophic balance. The past trajectory of
226 this anticyclone (black solid line in Figure 2) shows that it emerged from a meander of the
227 Algerian Current, which detached from the coast at 8°E and traveled up to the Sardinian coast.

228 This dynamical history shows that it can be classified as a typical AE. At this stage (Figure 2a), a
229 smaller anticyclonic structure seemed to appear at its northeast edge (39.5°N 6.8°E), but the
230 AMEDA algorithm did not identify it as a coherent eddy having closed streamlines.
231 Later, on 23 October, closed streamlines began to be detected around the small anticyclone and
232 on 27-28 October a *characteristic shared contour* (the green contour in Figure 2c) was identified
233 by the AMEDA algorithm. The formation of a new eddy simultaneously with the appearance of a
234 *characteristic shared contour* provided evidence for a splitting event (Le Vu et al., 2018). In
235 addition, the trajectory of the drifter, which passed from the initial AE to the new anticyclone
236 (red line in Figure 2c), confirmed the transfer of water mass between the two structures. The
237 dynamical core of the large AE fits well with the SST patterns (Figure 2b,d) even if the SST
238 signature of the small anticyclone was not as clear at this stage. However, analysis of the AVISO
239 geostrophic currents shows that the radius of this small anticyclone grew rapidly from ~20 km on
240 28 October to ~40 km on 8 November. Moreover, the surface drifter made several anticyclonic
241 loops around the new eddy center during the same period, thereby confirming the presence of the
242 anticyclonic structure.

243

244 Four months later, a few days before the survey, this mesoscale anticyclone shifted further to the
245 northwest following a clockwise path (Figure 2e,f). Its typical speed radius R_{\max} was still around
246 40 km and associated with ADT doming reaching 15 cm. The characteristic contour of the eddy
247 (blue line in Figure 2f) is in good agreement with the standard SST pattern of anticyclonic eddies
248 in winter, showing a warm SST anomaly (Puillat et al., 2002). At that time, the AE had moved
249 back to the Algerian coast following a cyclonic path in accordance with a two-gyre circulation of
250 the eddies depicted by Testor et al. (2005) and Escudier et al. (2016a). This eddy remained
251 coherent (it kept an anticyclonic core with closed streamlines) and interacted with the Algerian
252 Current inducing a very large meander along the coast that propagate eastward (Figure 2e).

253

254 3.2 Merging of the surveyed anticyclone with the Algerian eddy

255

256 The anticyclone surveyed at the end of March during the ProtevsMed 2016 cruise was detected
257 and tracked on the AVISO datasets until 4 May 2016. On 25 April, the structure was captured by
258 the drifters, which looped in its core (Figure 3a), and by the SST pattern (Figure 3 b), which
259 showed a cold circular anomaly with spiraling structures and stirred warm filaments especially
260 on its north side. However, despite its relatively large size, with a diameter being larger than 50
261 km (according to the drifter loops), the AVISO products combined with the AMEDA algorithm
262 did not detect the structure for one week. For instance, no closed streamlines were found at the
263 eddy location on 25 April (Figure 3a). This error in detection is mainly due to the lack of
264 altimetric tracks crossing the eddy area for almost 10 days.

265

266 The larger AE identified more southward (39°N 7°E) is a remnant of an AE persisting since the
267 previous November (year 2015), it interacted with the Algerian Current and partially detached

268 from the coast during the first two weeks of April with similar characteristics: a 25 cm ADT
269 dome and a characteristic radius R_{max} of around 45 km.

270

271 The monitored anticyclone (A) was detected again one week later, on 3 May 2016, with the
272 altimetric analysis. The characteristic contour (blue line in Figure 3c) given by the AMEDA
273 algorithm was slightly shifted compared with the drifter loops (Figure 3c) and the cold SST
274 anomaly (Figure 3d). A shared characteristic contour was also identified (closed green contour in
275 Figure 3c) on the geostrophic surface currents that encompassed both anticyclones. The
276 subsequent disappearance of the small anticyclone indicates that the latter merged back with the
277 AE.

278

279 This merging occurred rapidly (less than 10 days) and on 30 May (Figure 3e,f), the fusion was
280 complete and resulted in a wide anticyclonic structure that captured all the drifters. This fusion
281 confirms that the mass transfer from the small eddy to the large eddy was comprehensive. Hence,
282 the anticyclonic eddy (A) that split from an AE in October 2015 merged back with it seven
283 months later.

284

285 3.3 From warm core to cold core

286

287 In winter, AEs are characterized by warm surface cores of AW in a surrounding of colder water
288 masses. The present eddy was easily revealed before the field experiment as a warm patch on
289 remote-sensed data on 25 March (Figure 2f). This feature persisted during the cruise experiment
290 and the CTD casts did not exhibit any notable surface stratification in the eddy core.

291

292 In early spring, when the downwards atmosphere-ocean heat flux becomes positive again, the
293 upper seasonal thermocline tends to reduce the horizontal gradients of the sea surface
294 temperature induced by deep mesoscale eddies. On a contrary, eddy-wind interactions lead to a
295 total wind stress curl that favors upwelling (McGillicuddy et al., 2007). Gaube et al. (2014)
296 showed that this upwelling is associated with weaker downwelling, forming an antisymmetric
297 dipole in the core. Hence, both processes induce Ekman pumping inside the anticyclone and
298 therefore reduce (or delay) surface warming. This may explain why the anticyclones A (Fig 3a,
299 e) and AE (Figure 3e, f) appeared now as relative cold cores. Moreover, both the Rossby number
300 ($Ro=0.13$) and the relative core vorticity ($\zeta/f\sim-0.4$) of the anticyclone A reach non-negligible
301 values (see below paragraphs 4.3 and 4.5) and ageostrophic dynamics (Mahedevan et al., 2008)
302 may induces vertical mixing. The numerical simulation of Brannigan et al. (2016) and Zhong et
303 al. (2017), performed at very high resolution, also suggested that the surface wind-stress induces
304 ageostrophic instabilities in the mixed layer and initiate vertical mixing in anticyclonic eddies.
305 These ageostrophic and small scale process could also explain the relative cooling of surface
306 water inside the anticyclone.

307

308 **4 In situ observations and the dual-core vertical eddy structure**

309

310 4.1 Hydrographic transects

311

312 The first transect (GT1) crossed the eddy at its center and then revealed the main properties of
313 the eddy. It was composed of two very distinct water masses (A and A' in Figure 4) leading to a
314 negative anomaly of potential density. In the surface layer, the eddy was formed by a lens of AW
315 having a salinity of less than 37.75 and a potential temperature greater than 15°C. Near the core,
316 the thickness of this layer reached 150 m and the outer diameter of the eddy, estimated where
317 isopycnals intersect the surface, was in the range of 100-125 km. Next to the eddy center, under
318 this surface layer, a smaller hemispheric lens of cold water (less than 13.2°C) seemed trapped
319 under the surface structure. This water mass was also relatively fresh (salinity in the range of
320 37.90-38.2); it fell within the scope of WIW characteristics. The transition between the two
321 water masses was very thin and located at a depth of 180 m. On the GT1 transect, isopycnals
322 separating the two water masses were, nearly horizontal, indicating that under geostrophic
323 approximation, they spin together more or less at the same azimuthal velocity. Nevertheless, the
324 GT3 transect (central panels in Figure 4) showed a small slope for the isopycnals, suggesting
325 slight differences in azimuthal velocities.

326 Although this water mass did not have the typical characteristics of the WIW core (i.e. salinity
327 between 38.1 and 38.3 and temperature less than 13.0°C, according to Vargas-Yáñez et al.,
328 2012), this lens was obviously the result of a similar generating process. The winter cooling of
329 surface water in the northern part of the western Mediterranean Basin can isolate patches of
330 fresher and colder water from air-sea exchanges, WIW, allowing them to persist below the
331 surface layer for several months. The temperature and salinity of such patches depend on the
332 generation area and on the intensity of winter cooling. WIW formed on the shelf of the Gulf of
333 Lion or around the Ebro plume are fresher and colder than those formed along the offshore limit
334 of Northern Current or in the NBF.

335

336 In the western part of GT1 (5°E), small patches of WIW were located at 200 m depth with a
337 temperature similar to the eddy one, but with higher salinity (between 38.3-38.4).

338 The first half of the transect from the eddy boundary southwards (GT3) was very similar to the
339 GT1 transect. In the northern part of the GT3 transect, the eddy was in contact with a subsurface
340 cold water structure generated during the winter in the northern part of the western
341 Mediterranean Basin. This modal structure (weddy (W) shown in Figure 4) has been repeatedly
342 described in this area (Fuda et al., 2000; Goncharov et al., 2003) and appeared more clearly a
343 little bit later and a more eastwards in the RDT4 transect. The perturbation of the isopycnal
344 characterizes the anticyclonic behavior of the weddy (Bosse et al 2016). Northwards, near
345 40.9°N, an SCV induced a density perturbation down to at least 350 m. This SCV was a thin
346 anticyclone (diameter in the range of 20 km if the transect had crossed the center). Strikingly,
347 LIW ribbons were located on its flank with temperatures warmer than 13.5°C and salinity in the

348 range of 38.6 at a depth of 250-300 m. Around the eddy at 300 m depth, the top of the LIW layer
349 displayed increasing salinity around 38.5 and temperatures in the range of 13.4-13.5°C. Crossing
350 the NBF northwards, we therefore revealed a succession of anticyclones: an AE-like eddy
351 (diameter of about 80 km), a subsurface weddy (diameter of about 45 km) and an SCV (diameter
352 about 20 km), all interacting with each other.

353

354 4.2 Identification of water masses

355

356 The water masses present in this area were easily identifiable on the T/S diagram derived from
357 CTD casts (Figure 5). Unsurprisingly, there were four of them, namely:

- 358 • LIW characterized by an absolute maximum of salinity associated with a relative
359 maximum of temperature;
- 360 • Western Mediterranean Deep Water (WMDW);
- 361 • AW;
- 362 • WIWs of different characteristics.

363 The core LIW was present in the whole area between 400 and 500 m depth, even under the eddy
364 core where the maximum of salinity was deeper (600 m), in agreement with downwards convex
365 isopycnals frequently observed under anticyclonic structures. The characteristics of the LIW in
366 this area were a temperature around 13.5°C and salinity of the order of 38.6 for all CTD cast
367 profiles. Under the eddy, the LIW layer was saltier and thicker. Because the isopycnals
368 corresponding to the LIW were convex, the rotation induced Potential Vorticity patterns that
369 preserved the rotating water bodies from surrounding environment where LIW were less marked
370 and more mixed.

371

372 At a depth of 800 m, the eddy no longer affected potential density, although temperature and
373 salinity remained affected down to 1200 m. The WMDW characteristics showed temperatures of
374 less than 12.9°C and salinity of less than 38.5 in the deeper part of the profile. In the last 500 m
375 above the seafloor this water mass exhibited a slight increase in salinity and temperature (not
376 shown) due to the southward migration of deep-convected water in the Gulf of Lion.

377

378 The WIW present in the eddy core appeared very clearly in the TS diagram (Figure 5), with a
379 near-core profile showing a very marked water mass with a temperature of 13.15°C and salinity
380 of 38.05°C. This isolated water mass was present only in the eddy core, but WIWs with other
381 characteristics were present around the eddy and also appeared on the TS diagram as denser,
382 with less marked minima of temperature and salinity in the range of 38.25-38.45.

383

384 4.3 Velocity measurements inside the anticyclone

385

386 Using the high-resolution SeaSoar transect (a mean distance of 1200 m between the rising and
387 descending oscillation), we derived geostrophic currents from the density profiles. To do so, we
388 assumed that the SeaSoar oscillations were vertical. The measured density profiles were then

389 used to derive, according to the thermal wind equation, the transverse geostrophic velocity,
390 considering the deepest level at 325 m as a zero velocity level. The geostrophic velocity section
391 along the GT1 transect (Figure 6b) shows a surface-intensified eddy with a maximal intensity in
392 the range of 40 cm/s in the surface layer. The eddy center, where the azimuthal velocity
393 vanished, was estimated to be near 5.75°E and the maximal values were reached at 5.35°E and
394 6.1°E. The estimated speed radius R_{\max} was then around 32 km and the corresponding Rossby
395 number ($Ro = V_{\max} / (f R_{\max})$ where f is the Coriolis parameter at the eddy latitude; at 40°N, $f =$
396 $0.937 \cdot 10^{-4} \text{ s}^{-1}$) ~ 0.13 . The comparison with the AVISO geostrophic velocities along the same
397 transect is plotted in Figure 6a and shows that the meridional component of the surface velocity,
398 derived from altimetry, corroborates the geostrophic velocity (at 50 m), derived from the thermal
399 wind equation. However, as discussed in section 2.1, the characteristic speed radius R_{\max} appears
400 to be overestimated in the AVISO dataset.

401 On the GT3 transect (half the north-south diameter), two independent velocity estimations were
402 performed (Figure 7). First, the zonal (azimuthal) current was interpolated from 10 LADCP
403 measurements taken during the CTD casts. Second, the zonal geostrophic velocities were
404 estimated from the GT3 SeaSoar transect with a reference level of 360 m. The zonal geostrophic
405 current was also derived from the CTD profiles with a more reliable reference level of 1500 m
406 (not shown). All velocity estimations exhibited the same pattern and roughly the same amplitude
407 (up to 40 cm/s), thereby corroborating these independent velocity evaluations. The center of the
408 anticyclone was estimated at around 39.9°N and the eddy extended up to 40.5°N with surface-
409 intensified velocities.

410 A secondary intensified region corresponded to the WIW lens between 160 and 300 m depth. On
411 the LADCP data, the rotation axis (A') of the WIW lens was not aligned with the rotation axis
412 (A) of the AW lens and appeared to be shifted southward. This feature was confirmed by the
413 SeaSoar-estimated velocities that showed the same behavior near the core as in the GT1 transect.
414 Under the surface eddy boundary, the zonal current revealed a secondary circulation pattern at
415 the subsurface, at a depth greater than 100-150 m. At 40.45°N, the current flowed westwards
416 driven by the anticyclone of modal water (W), centered at 40.55°N described above (Figure.
417 4b,c).

418

419 4.4 Interaction with the North Balearic Front

420

421 In March, the eddy moved northwestwards until it reached the Balearic Front and interacted with
422 the colder water located behind the front. The two anticyclonic structures A and W likely
423 interacted with each other, as revealed by the vertical shear located at 40.4°N and at a depth of
424 75 m on the LADPC recorded velocities (Figure 7a). Using kriging techniques, an approximation
425 of the horizontal temperature field at 75 m depth was deduced from all the SeaSoar transects
426 (Figure 8a). The anticyclonic eddy (A) was identified at 75 m deep by a patch of warm water
427 centered near 5°40'W 39°55'N; the second anticyclone (W) appeared as a cold (and smaller)
428 patch centered near 5°40'W 40°30'N and was a modal structure composed of WIW. The 10 direct

429 LADCP velocity measurements at 75 m depth were interpolated along the 5°40'N (GT3) transect
430 and indicated that some of the subsurface eddy water mass was caught by the weddy-induced
431 circulation. Above the modal water vortex W, an anticyclonic wrap of surface AW was trapped
432 by the weddy and detached from eddy A (Figure 8b). Evidence for this process was also clear on
433 the RDT4 transect (Figure 4); the AW wrapped over the weddy appeared on the surface near
434 41°N as warm and fresh water filaments. Weddies are ubiquitous, at least during winter and
435 spring in the NBF, and often appear as cold-core anticyclones on remote-sensed SST data, e.g.
436 during the cruise for the month of March 2016 (x in Figure 8b). This eddy-weddy interaction
437 leads to a net transport of AW across the NBF, giving some buoyancy to the Northern Gyre and
438 feeding, with the West and East Corsica Currents, the density dynamics of the northwestern
439 Mediterranean Basin.

440

441 4.5 Lagrangian velocities and drifting buoys

442

443 To estimate the rotation within the eddy core and the drifting speed of the anticyclone, four SVP-
444 type drifters, with a 50 m depth holey sock, were dropped near the eddy center on 29 March. The
445 four drifters remained trapped in the eddy for almost one month with very similar trajectories
446 (Figure 9a). The average rotation period deduced from the latitudinal or longitudinal
447 displacement (Figure 9c,d) was in the range of 4 days. The Lagrangian velocities varied from 0.1
448 to 0.7 m/s with a mean value of around 40 cm/s after 4 April (Figure 9b). Early May, the drifters
449 exited from the surveyed anticyclone and were caught by the larger AE located south as shown
450 in the eddy tracking (Figure 3).

451

452 Given that the tracks were elliptic and the horizontal flux was assumed almost non-divergent, the
453 drifter velocities increased when crossing the semi-minor axis (northernmost or southernmost
454 position) and decreased when crossing the semi-major axis (westernmost or easternmost
455 position). Moreover, at the beginning of the track, drifters were closer to the eddy center and
456 obviously moved slower (0.1-0.2 m/s). All drifters decelerated on 9 April when the eddy rapidly
457 drifted southwards and then eastwards.

458 Assuming the eddies are ellipses that vary continuously in size, shape and position, it is possible
459 to extract geometrical properties of the track as instantaneous virtual streamlines from the x-y
460 displacements of drifters (Lilly & Gascard, 2006; Brassington, 2006; Paillet et al., 2002).
461 Therefore, the mean (averaged over one rotation period) position and velocity of the eddy center
462 are available as the mean velocity or mean distance of the drifter from the idealized eddy center.

463 The four buoys drifted away from the center during the five first days. The mean radius
464 increased, indicating a divergence in the surface layer (Figure 9e) and the radial velocity was
465 approximately 0.04 m/s. The drifters remained trapped inside the eddy for one month at a radius
466 of 24 km, corresponding to the size of the homogeneous AW layer at 50 m depth (the mean
467 depth of the holey sock). The ratio of the mean azimuthal velocity with respect to the mean
468 radius was nearly constant for drifting buoys in the eddy (Figure 9f). For all drifters, the slopes
469 of V_{mean} plotted against R_{mean} remained almost constant in the eddy core, with a value of around

470 $0.18 \cdot 10^{-4} \text{ s}^{-1}$ (e.g. a mean azimuthal velocity of 0.40 m/s for a mean radius of 22 km). The eddy
 471 ellipticity ε was deduced from the drifter trajectories and remained weak $\varepsilon \sim 0.2$. Hence,
 472 assuming a quasi-circular shape, we estimated the relative core vorticity at $\zeta_0/f = 2 V_{\text{mean}}/(f R_{\text{mean}})$
 473 ~ -0.42 , with $f = 0.937 \cdot 10^{-4} \text{ s}^{-1}$. According to this value (greater than the critical value $\zeta_0/f = -1$),
 474 the potential vorticity remained positive and this mesoscale anticyclone cannot be affected by
 475 unstable inertial perturbations (Kloosterziel, et al., 2007; Lazar et al., 2013a, 2013b). It may
 476 therefore remain stable and coherent for several months. Nevertheless, the negative core vorticity
 477 was not negligible and the eddy was at the limit of validity for the geostrophic balance. The
 478 centrifugal terms were no longer negligible and some secondary ageostrophic dynamics
 479 (Mahedevan et al., 2008) may occur.

480 The azimuthal velocity profile derived by the AMEDA algorithm from the AVISO geostrophic
 481 velocities (gray curve on Figure 9f) underestimated the in situ drifter velocities. Similar
 482 underestimation of surface currents derived from gridded altimetric maps in comparison with in
 483 situ measurements have been reported for the North Atlantic (Fratantoni, 2001), the Alboran
 484 Gyre (Juza et al., 2016) and the Ierapetra anticyclone (Ioannou et al., 2017), due to filtering,
 485 smoothing and optimal interpolation of altimetric data. The position of the eddy center inferred
 486 from the AMEDA tracking tools corresponds to that deduced from the drifting buoy analysis
 487 (Figure 9a,c,d). When the eddy moved eastward (between 15 and 25 April), it escaped for 10
 488 days the altimeter tracks, and thus optimal interpolation and no positions were calculated.

489

490 4.6 Observation of submesoscale and fine-scale structures

491

492 SeaSoar transects and vertical profiles showed fine-scale structures inside or around the eddy
 493 exhibiting secondary motions at small scales, below the deformation radius. Already observable
 494 in hydrological transects (Figure 4), some small vertical-scale features can be highlighted by
 495 drawing the non-dimensional spice variable defined as:

496

$$497 \quad s = \alpha(T - T_0) + \beta(S - S_0),$$

498

499 where α, β, T, S are respectively the thermal expansion coefficient, the haline contraction
 500 coefficient, the potential temperature and the salinity of seawater. S_0 and T_0 are reference
 501 temperature and salinity. Spice behaves as a passive tracer and can reveal secondary circulation
 502 patterns not directly driven by the mean density field. This variable highlights the submesoscale
 503 structures inside and around eddies (L'Hégaret et al., 2016 ; Pietri & Karstensen, 2018).

504

505 Inside the eddy core, in the AW layer just below the surface Ekman layer, three or four cells of
 506 less spicy water were detected between 50 m and 120 m deep (blue dots in Figure 10a). These
 507 cells corresponded also to patch of chlorophyll a (chl *a*) (Figure 10b). They are separated by
 508 vertical plumes of more spicy water and of lower biological productivity. This particular pattern,
 509 already revealed on the temperature field and less obviously on the salinity field (Figure 4), was

510 robust. These cells were similarly present on all other transects, suggesting a horizontal annular
511 or spiraling shape. Vertical exchange between the top and the bottom of the eddy core is obvious,
512 but the spice isopleths did not follow the isopycnals, and there is no evidence for intense
513 convection. Assuming the eddy cores were not exactly in solid rotation, stirring of the
514 upwelling/downwelling dipole may lead to this pattern. Alternatively, these observations are
515 consistent with a study that showed, based on measurements and modeling, small-scale
516 variations in strain, divergence and vorticity in the eddy core (Zhong et al., 2017). A numerical
517 study (Brannigan, 2017) showed similar vertical structure of a passive tracer in the eddy core
518 with a decrease in grid size to 250 m. Both studies attributed the small-scale vertical structures to
519 mixed layer instability and ageostrophic dynamics.

520 The second striking small-scale observations involve the “arms” encompassing the WIW part of
521 the eddy and more noticeable at its western boundary. These structures were also present in other
522 eddy transects. The arms (plumes of more spicy water denoted ‘a-a’, b-b’, c-c’, d-d’, e-e’, Figure
523 10) clearly crossed the isopycnals and were roughly aligned on an azimuthal velocity gradient
524 (see Figure 6). Therefore, passive stirring by the geostrophic velocity field may be involved. Due
525 to the horizontal gradients of seawater properties (the NBF) or in the presence of patches of
526 different water masses, the shear of azimuthal velocity can generate layering aligned on a
527 velocity gradient. A study on the layering formation in a modal structure suggests that the
528 variability due to vortex instabilities is able to initiate the stirring process, leading to the
529 prediction that layering under surface-intensified vortices occurs (Meunier et al. (2014).

530 Patchiness of phytoplankton also revealed submesoscale processes in the surface and subsurface
531 layers. Fluorescence is a proxy for the estimation of chl *a* concentrations and phytoplankton
532 abundance (Figure 10b). Inside the eddy core, the phytoplankton was strictly confined to the first
533 150 m, corresponding to mixed and ventilated AW layer, with a subsurface maximum located at
534 around 75 m depth. Patches of phytoplankton corresponded to spice structures. Dynamically
535 isolated from the surface and located under the euphotic layer, the core of WIW is logically not
536 involved in primary production. In contrast, the eddy boundaries, where isopycnals outcrop, were
537 in an area of stronger primary production generated by vertical fluxes of nutrients and
538 phytoplankton. Among the processes involved, the interaction of the eddy velocity and structures
539 with wind stress and air-sea exchanges may generate symmetric instabilities leading to a spatial
540 succession of upwelling and downwelling along the frontal area (Brannigan, 2016). The
541 observations in the present eddy are in agreement with these hypotheses, because the plumes of
542 phytoplankton were found along isopycnals near the eddy boundaries.

543

544 The CTD casts 14 and 15 were both located in the core, along the GT3 transect where the two
545 components of the eddy (AW and WIW) lenses were superimposed (figure 11). As expected, the
546 Brunt-Väisälä frequency was very high (greater than f) between the two water masses, thereby
547 inhibiting vertical exchange of salt, heat and momentum and preserving the two-layer structure
548 of the anticyclone from diapycnal mixing. The thickness of this layer was roughly 50 m (yellow-
549 shaded area in Figure. 11). Vertical profiles of current were recorded with the LADCP. The data

550 collected during the raising and lowering of the current profiler show striking features in this
551 transition area. The zonal velocity (here, the azimuthal velocity in the eddy frame) was weaker
552 than that of the two adjacent water masses. On CTD 14, the azimuthal velocity even vanished in
553 this zone. This azimuthal velocity was not exactly identical in the AW and WIW lenses, as
554 | already suggested by the $-v$ velocity estimations (Figures 6 and 7). The current in the deeper
555 structure was slightly stronger. The meridional velocity (here, the radial velocity in the eddy
556 frame) remained weak or nil as expected in classical eddy models, but reached a maximum in the
557 area of increased Brunt-Väisälä frequency. The current veering suggests that this layer acts as an
558 Ekman layer between the two water masses spinning together in the same way but with different
559 velocities and probably misaligned rotation axes. The two parts of the eddy were dynamically
560 uncoupled in terms of heat, salt and momentum exchange.

561

562 **5 Discussion: where does the cold subsurface water inside the anticyclone come from?**

563

564 As shown above, the surface layer of eddy AA' was clearly formed from AW, which regularly
565 stays in the Algerian Basin, south of the NBF. The WIW found below the AW was formed in the
566 northern part of the Algerian Basin, north of the NBF. This unexpected cold patch embedded
567 under a relatively typical eddy required further investigation.

568 We explored all Argo float data (35,529 profiles), glider data (72,007 profiles), CTD casts (3621
569 profiles) and thermosalinograph (TSG) transects available for the western Mediterranean Sea in
570 the Coriolis database (<http://www.coriolis.eu.org>). Looking for the water mass encompassing all
571 types of WIW (potential temperature less than 13.2°C; salinity less than 38.2) showed that WIW
572 masses were found at various depths (mainly at 20-50 m) in the Gulf of Lion, in the North
573 Current, north of the Balearic Islands and along the NBF (Figure 12). In the southern part of the
574 basin, WIW was sporadically found deeper, between 120 m and 250 m, as modal waters. Two
575 paths of southward migration of WIW appeared in the data: the first path goes through the Ibiza
576 Channel as already discussed by Pinot & Ganachaud. (1999); the second path crosses the NBF
577 east from Minorca as modeled by Juza (2013).

578

579 There are at least three processes that may be involved in the formation of this singular structure.

580

581 The first process assumes that WIW is already present under the Algerian Current, as
582 sporadically observed (Benzohra et al., 1995a;1995b), and is caught by the eddy during its
583 formation. Thereafter, this double eddy follows a typical path until it reaches the NBF, east of
584 Minorca Island. However, despite one unique report, WIW is generally not found close to the
585 Algerian coast.

586

587 Second, the formation of WIW during winter is not the result of classical convection generated
588 by static instability leading to vertical motion in convective plumes, thereby enhancing strong
589 vertical and horizontal mixing. Instead, WIW appears to plunge along the isopycnal surfaces and
590 preserve the characteristics of its water mass, involving a symmetric instability process. The

591 main part of the WIW is known to be formed by frontal dynamics along the North Current and
592 the Balearic Fronts. Nevertheless, in this context, anticyclonic eddies in the NBF are particularly
593 predisposed to subduction processes as isopycnals outcrop. The WIW may plunge under an
594 anticyclonic eddy in the Balearic Front during strong convection events (mistral gusts in
595 February or March), as observed during last HYMEX experiment, in glider tracks in 2013 (see
596 Figure 6 in Estournel et al., 2016). However, winter 2015-2016 was too mild to generate such
597 WIW characteristics (no sufficiently low temperatures were recorded by infrared images).
598 Therefore, although this process deserves mention, it cannot have occurred for this eddy.

599

600 The third process assumes the vertical alignment of an Algerian surface eddy formed from AW
601 with a subsurface weddy, formed from WIW. Weddies are frequently observed north of the NBF
602 and are found to move towards the Algerian Basin across the Balearic Straits. Although a few
603 recent eddy tracking algorithms have detected merging events between surface eddies (Yi et al.,
604 2014; Li et al., 2014; Le Vu et al., 2018), the merging or alignment between a surface eddy and
605 a subsurface lens cannot usually be detected with remote-sensing observations. Hence, such
606 vertical alignment can happen even if we have no evidence of its creation.

607 The coalescence of two anticyclonic structures has rarely been observed in situ. Cresswell (1982)
608 demonstrated the coalescence of two anticyclonic eddies having different thicknesses and depths
609 along the southwestern coast of Australia. The water mass of each structure was characterized
610 during the first cruise leg and retrieved in the final structure during the second leg. The CTD cast
611 in the final anticyclone exhibited a dual-core structure similar to the one we observed here. In the
612 same area, Baird et al. (2012) described dual-core eddies formed on the surface by water from
613 the unstable East Australian Current and in subsurface by denser water from Bass Strait. In a
614 stratified rotating flow, anticyclonic vortices of different densities tend to align vertically (Nof &
615 Dewar, 1994), further supporting this assumption of vertical alignment of two separate
616 structures.

617 Interestingly, the careful examination of all profiles available in the northwestern Mediterranean
618 Sea in the Coriolis database revealed only one series of TS profiles from an SCV that is
619 consistent with the WIW characteristics present in the lower layer of the eddy (Figure 12b). It
620 was found in the Algerian Basin (5°W 38.5°N) in July 2015, eight months before our observation
621 in March 2016, in an area affected by the dynamics of the larger southern AE (Figure 2).
622 Unfortunately, no surface signature in sea surface height nor in SST was associated with this
623 internal structure and the profiles did not show any surface density anomaly related to surface
624 structure. This SCV is nevertheless a good candidate for an alignment with a surface AE in the
625 Algerian Basin, providing further support for the assumption of a coalescence process.

626

627 **6 Conclusions**

628

629 A high-resolution survey of an Algerian Eddy revealed an unexpected, dual-core eddy. Under the
630 AE surface composed of AW, we found a coherent WIW water mass. These two water masses
631 that rotate together in the same dynamical structure are not coupled by friction.

632 Tracking this surface eddy from its birth – upon splitting from a bigger AE – to its death – upon
633 merging –, and examining all Argo drifters available in the western Mediterranean Sea, revealed
634 an SCV in the Algerian basin, close to the past eddy trajectory, with the appropriate WIW
635 characteristics. Our investigations suggest that an alignment of this SCV with an AE is the origin
636 of this dual core eddy.

637

638 AEs composed of AW have been also associated with westward transportation of LIW in the
639 Algerian basin. Because LIW exists as modal structures in the western Mediterranean Sea, the
640 same vertical alignment with LIW can be expected.

641

642 Using high-resolution sampling, submesoscale features have been pointed out in observations,
643 related to stirring when aligned on geostrophic velocity gradients or related to symmetric
644 instability when aligned on outcropped isopycnals. The processes leading to the submesoscale
645 observations described in this study are still under debate. Unfortunately, the lack of fine-scale
646 azimuthal and radial velocity measurements hinders any further data interpretation. We
647 illustrated that it is possible to carry out synoptic and in situ measurements of the submesoscale
648 structure. More simultaneous measurements at both mesoscale and submesoscale should be
649 generalized in future campaigns in order to validate and tune numerical simulations of the
650 internal eddy dynamics at very high resolution.

651

652 The NBF is not only a surface and seasonal front, but also it clearly separates the Algerian Basin
653 from the Northern Gyre dynamics. Nevertheless, this front is not hermetic and mesoscale
654 processes can enhance cross-front exchanges. Due to partial convection and surface water
655 subduction, anticyclones also stay in the northern and denser part of the front as modal water
656 structures. Called weddies, or SCVs when smaller, such winter-formed water migrates towards
657 the NBF and sometimes penetrates the Algerian Basin. Close to the front, they are able to catch
658 surface AW and then bring buoyancy to the general cyclonic dynamics encompassing the
659 northwestern Mediterranean Basin. Due to the occurrence of strong mesoscale and submesoscale
660 dynamics in a context of contrasted and well-defined water masses, the NBF provides the perfect
661 setting for investigating small-scale interactions, associated ageostrophic motion and energy
662 cascades.

663

664

665

666

667 **Figure captions**

668

669 Figure 1. Eddy signatures on the SST scene from a Metop/AVHRR/3 radiometer (29 March
670 2016). The eddy center (blue star) and the contour of maximum velocity (solid blue line) were
671 both inferred from the AVISO datasets, according to the AMEDA algorithm. The SeaSoar
672 transects are indicated with black lines. Drifter release positions are shown (light blue circles).
673 The crosses (x) indicate CTD cast positions and the red lines show the ship track. The situation
674 box represents the position of the eddy in the northwestern Mediterranean Sea (blue square). The
675 mean position of North Balearic Front (NBF) is drawn (red dotted line). All in situ data were
676 recorded from 27 March to 1 April.

677

678 Figure 2. Eddy behavior before the field experiment.. Left column: Absolute dynamical
679 topography (color), geostrophic currents (black arrows) and characteristic contours (blue and red
680 lines) of the eddies detected by AMEDA plotted together. The trajectories of the Algerian eddy
681 (AE) and the surveyed anticyclone (A) are depicted by a thick black line and the positions of
682 drifting buoys (red circles) during the previous 15 days are shown (from dark red at on day 0 to
683 white at on day -15). Right column: Sea surface temperature (VIIRS/ Suomi-NPP) and the
684 characteristic contours (blue: anticyclones, red: cyclones) of the eddies detected by AMEDA.

685

686 Figure 3. Eddy behavior after the field experiment.. Right column: Absolute dynamical
687 topography (color), geostrophic currents (black arrows) and characteristic contours (blue and red
688 lines) of the eddies detected by AMEDA plotted together. The trajectories of the Algerian eddy
689 (AE) and the surveyed anticyclone (A) are depicted by a thick black line and the positions of
690 drifting buoys (red circles) during the previous 15 days are shown (from dark red at day 0 to
691 white at -15 days). Left column: Sea surface temperature (VIIRS/ Suomi-NPP) and the
692 characteristic contours (blue: anticyclones, red: cyclones) of the eddies detected by AMEDA.

693

694 Figure 4. Temperature (left panels) and salinity (right panels) vertical cross-sections along
695 transects GT1 (28 March), GT3 (28 March 28) and RDT4 (30 March) from top to bottom
696 respectively. White lines indicate density anomalies plotted every 1 kg/m^3 (thick) or 0.25 kg/m^3
697 (thin). CTD and LADCP measurements along GT3 are reported (13 to 22) but not used for
698 interpolation. AA' indicates the surveyed eddy, W the adjacent weddy and SCV the
699 northernmost sub-coherent vortex.

700

701 Figure 5. CTD casts along a north-south transect in the eddy. The light blue profile is located in
702 the eddy core, the dark blue profile (CTD 14) near the eddy boundary (CTD 16) and the red
703 profile in surrounding waters (CTD 21). (See Figures 1 and 4 for CTD positions). (a) Salinity
704 and potential temperature profiles, (b) potential density, (c) TS diagram. The green-shaded area
705 corresponds to the WIW layer near the eddy center. The grey curves on TS-diagram correspond
706 to all others CTD cast of the transect.

707

708 Figure 6. (a) Geostrophic velocity along the GT1 transect deduced from AVISO field derived
709 surface slope (dots) compared with geostrophic velocity at 50 m depth deduced from density
710 field with a reference level at 325 m) (b) Geostrophic velocity along the GT1 transect.

711

712 Figure 7. Velocities along the north-south transect (GT3) deduced from direct measurement by
713 LADCP (a), from the thermal wind equation using the SeaSoar transect with a reference depth of
714 360 m (b). CTD and LADCP stations are designated from 0013 to 0022.

715

716 Figure 8. (a) Temperature at 75 m. Gray lines are positions of data taken into account for kriging.
717 Currents at 75 m were interpolated from LADCP measurements. (b) Sea surface temperature on
718 30 March 2016. The positions of suspected weddies, associated with clockwise surface AW
719 advection are indicated (x and dashed arrows).

720

721 Figure 9. (a) Trajectories of the drifters dropped near the eddy core; dashed lines represent the
722 track of the eddy center. (b) Lagrangian velocity experienced by the drifters from 29 March to 5
723 May; black dashed lines represent the velocity averaged over a rotation period. (c) Longitudinal
724 and (d) latitudinal displacement of the drifters; the dashed line represents the motion of the eddy
725 center. (e) Mean radius averaged over a rotation period. (f) Mean azimuthal velocity against
726 mean radius. Colored lines denote the four dropped drifters; gray curve in (d) is the characteristic
727 of the eddy deduced from AMEDA for 31 March. Gray stars on (a)(c)(d) denote the eddy center
728 inferred from AMEDA tracking tool.

729

730 Figure 10. Non-dimensional spice variable (a) and decimal log of chlorophyll *a* (b) along the
731 GT1 transect.

732

733 Figure 11. Brunt-Väisälä frequency (N/f) and velocity profile from LADCP measurements in the
734 eddy core for CTD 14 and CTD 15 (see Figures 4 and 7 for position). The yellow-shaded area
735 corresponds to the transition layer between the AW and the WIW parts of the eddy.

736

737 Figure 12. (a) Argo drifters, CTD, glider profiles and surface thermosalinograph positions in the
738 western Mediterranean Sea from 1995 to 2016 (gray dots) in the Coriolis database. When WIW
739 (potential temperature $< 13.2^{\circ}\text{C}$ and salinity < 38.2) is present, the mean depth of this water mass
740 layer is shown. (b) Temperature-salinity (TS) diagram from an ARGO profiler at 38.2°N 5°E in
741 July 2015 (white circle), gray dots are the TS diagrams of the CTD casts in the eddy recorded in
742 March 2016.

743

744 Acknowledgments

745 The authors acknowledge the financial support of the French Government Defense procurement
746 and technology agency (DGA) through the PROTEVS project and the French National Research
747 Agency (ANR)-Astrid project DYNED-Atlas (ANR-15-ASMA-0003-01). They thank the
748 technical team at the French Naval Hydrologic and Oceanographic Service (SHOM), the crew of

749 the French Navy ship *Beautemps-Beaupré* for their contribution to the field experiment and the
750 AVISO center for providing the surface geostrophic currents. Raw data are available on Seanoce
751 data repository at: <http://doi.org/10.17882/56028>

752

753 References

- 754 Allen, J. T., Painter, S. C., & Rixen, M. (2008). Eddy transport of Western Mediterranean
755 Intermediate Water to the Alboran Sea. *Journal of Geophysical Research: Oceans*, *113*(C4),
756 C04024. <https://doi.org/10.1029/2007JC004649>
- 757 Amitai, Y., Lehahn, Y., Lazar, A., & Heifetz, E. (2010). Surface circulation of the eastern
758 Mediterranean Levantine basin: Insights from analyzing 14 years of satellite altimetry data.
759 *Journal of Geophysical Research: Oceans*, *115*(C10), C10058.
760 <https://doi.org/10.1029/2010JC006147>
- 761 Baird, M. E., & Ridgway, K. R. (2012). The southward transport of sub-mesoscale lenses of
762 Bass Strait Water in the centre of anti-cyclonic mesoscale eddies. *Geophysical Research Letters*,
763 *39*(2), L02603. <https://doi.org/10.1029/2011GL050643>
- 764 Benzohra, M., & Millot, C. (1995a). Characteristics and circulation of the surface and
765 intermediate water masses off Algeria. *Deep Sea Research Part I: Oceanographic Research*
766 *Papers*, *42*(10), 1803–1830. [https://doi.org/10.1016/0967-0637\(95\)00043-6](https://doi.org/10.1016/0967-0637(95)00043-6)
- 767 Benzohra, M., & Millot, C. (1995b). Hydrodynamics of an open sea Algerian eddy. *Deep Sea*
768 *Research Part I: Oceanographic Research Papers*, *42*(10), 1831–1847.
769 [https://doi.org/10.1016/0967-0637\(95\)00046-9](https://doi.org/10.1016/0967-0637(95)00046-9)
- 770 Bosse, A., Testor, P., Houpert, L., Damien, P., Prieur, L., Hayes, D., ... Mortier, L. (2016).
771 Scales and dynamics of Submesoscale Coherent Vortices formed by deep convection in the
772 northwestern Mediterranean Sea. *Journal of Geophysical Research: Oceans*, *121*(10), 7716–
773 7742. <https://doi.org/10.1002/2016JC012144>
- 774 Brannigan, L. (2016). Intense submesoscale upwelling in anticyclonic eddies. *Geophysical*
775 *Research Letters*, *43*(7), 2016GL067926. <https://doi.org/10.1002/2016GL067926>
- 776 Brannigan, L., Marshall, D.P., Naveira Garabato, A.C., Nurser, A.J.G., Kaiser, J., 2017.
777 Submesoscale Instabilities in Mesoscale Eddies. *J. Phys. Oceanogr.* *47*, 3061–3085.
778 <https://doi.org/10.1175/JPO-D-16-0178.1>
- 779 Brassington, G. B. (2009). Estimating Surface Divergence of Ocean Eddies Using Observed
780 Trajectories from a Surface Drifting Buoy. *Journal of Atmospheric and Oceanic Technology*,
781 *27*(4), 705–720. <https://doi.org/10.1175/2009JTECHO651.1>
- 782 Chelton, D. B., Schlax, M. G., & Samelson, R. M. (2011). Global observations of nonlinear
783 mesoscale eddies. *Progress in Oceanography*, *91*(2), 167–216.
784 <https://doi.org/10.1016/j.pocean.2011.01.002>
- 785 Cotroneo, Y., Aulicino, G., Ruiz, S., Pascual, A., Budillon, G., Fusco, G., & Tintoré, J. (2016).
786 Glider and satellite high resolution monitoring of a mesoscale eddy in the algerian basin: Effects

- 787 on the mixed layer depth and biochemistry. *Journal of Marine Systems*.
788 <https://doi.org/10.1016/j.jmarsys.2015.12.004>
- 789 Cresswell, G. R. (1982). The Coalescence of Two East Australian Current Warm-Core Eddies.
790 *Science*, 215(4529), 161–164. <https://doi.org/10.1126/science.215.4529.161>
- 791 Escudier, R., Mourre, B., Juza, M., & Tintoré, J. (2016a). Subsurface circulation and mesoscale
792 variability in the Algerian subbasin from altimeter-derived eddy trajectories. *Journal of*
793 *Geophysical Research: Oceans*, 121(8), 6310–6322. <https://doi.org/10.1002/2016JC011760>
- 794 Escudier, R., Renault, L., Pascual, A., Brasseur, P., Chelton, D., Beuvier, J., 2016b. Eddy
795 properties in the Western Mediterranean Sea from satellite altimetry and a numerical simulation.
796 *Journal of Geophysical Research: Oceans* 121, 3990–4006. <https://doi.org/10.1002/2015JC011371>
- 797 Estournel, C., Testor, P., Taupier-Letage, I., Bouin, M.-N., Coppola, L., ... Somot, S. (2016).
798 HyMeX-SOP2: The Field Campaign Dedicated to Dense Water Formation in the Northwestern
799 Mediterranean. *Oceanography*, 29(4), 196–206. <https://doi.org/10.5670/oceanog.2016.94>
- 800 Font, J., Isern-Fontanet, J., & Salas, J. D. J. (2004). Tracking a big anticyclonic eddy in the
801 western Mediterranean Sea. *Scientia Marina*, 68(3), 331–342.
- 802 Forryan, A., Allen, J. T., Edhouse, E., Silburn, B., Reeve, K., & Tesi, E. (2012). Turbulent
803 mixing in the eddy transport of Western Mediterranean Intermediate Water to the Alboran Sea.
804 *Journal of Geophysical Research: Oceans*, 117(C9), C09008.
805 <https://doi.org/10.1029/2012JC008284>
- 806 Fratantoni, D. M. (2001). North Atlantic surface circulation during the 1990's observed with
807 satellite-tracked drifters. *Journal of Geophysical Research: Oceans*, 106(C10), 22067–22093.
808 <https://doi.org/10.1029/2000JC000730>
- 809 Fuda, J. L., Millot, C., Taupier-Letage, I., Send, U., & Bocognano, J. M. (2000). XBT
810 monitoring of a meridian section across the western Mediterranean Sea. *Deep Sea Research Part*
811 *I: Oceanographic Research Papers*, 47(11), 2191–2218. [https://doi.org/10.1016/S0967-](https://doi.org/10.1016/S0967-0637(00)00018-2)
812 [0637\(00\)00018-2](https://doi.org/10.1016/S0967-0637(00)00018-2)
- 813 Gaube, P., Chelton, D. B., Samelson, R. M., Schlax, M. G., & O'Neill, L. W. (2014). Satellite
814 Observations of Mesoscale Eddy-Induced Ekman Pumping. *Journal of Physical Oceanography*,
815 45(1), 104–132. <https://doi.org/10.1175/JPO-D-14-0032.1>
- 816 Goncharov, V. V., Yu, A., Chepurin, A., & Aleinik, D. L. (2003). Experimental Study of an
817 Intrathermocline Mediterranean Water Lens and Possibilities of Its Remote Detection. *Izvestiya,*
818 *Atmospheric and Oceanic Physics*, 39(5), 614–623.
- 819 Ioannou, A., Stegner, A., Le Vu, B., Taupier-Letage, I., & Speich, S. (2017). Dynamical
820 Evolution of Intense Ierapetra Eddies on a 22 Year Long Period. *Journal of Geophysical*
821 *Research: Oceans*. <https://doi.org/10.1002/2017JC013158>
- 822

- 823 Isern-Fontanet, J., García-Ladona, E., & Font, J. (2006). Vortices of the Mediterranean Sea: An
824 Altimetric Perspective. *Journal of Physical Oceanography*, *36*(1), 87–103.
825 <https://doi.org/10.1175/JPO2826.1>
- 826 Juza, M., Renault, L., Ruiz, S., & Tintoré, J. (2013). Origin and pathways of Winter Intermediate
827 Water in the Northwestern Mediterranean Sea using observations and numerical simulation.
828 *Journal of Geophysical Research: Oceans*, *118*(12), 6621–6633.
829 <https://doi.org/10.1002/2013JC009231>
- 830 Juza, M., Moure, B., Renault, L., Gómara, S., Sebastián, K., Lora, S., ... Tintoré, J. (2016).
831 SOCIB operational ocean forecasting system and multi-platform validation in the Western
832 Mediterranean Sea. *Journal of Operational Oceanography*, *9*(sup1), s155–s166.
833 <https://doi.org/10.1080/1755876X.2015.1117764>
- 834 Kloosterziel, R. C., Carnevale, G. F., & Orlandi, P. (2007). Inertial instability in rotating and
835 stratified fluids: barotropic vortices. *Journal of Fluid Mechanics*, *583*, 379–412.
836 <https://doi.org/10.1017/S0022112007006325>
- 837 Lazar, A., Stegner, A., & Heifetz, E. (2013a). Inertial instability of intense stratified
838 anticyclones. Part 1. Generalized stability criterion. *Journal of Fluid Mechanics*, *732*, 457–484.
839 <https://doi.org/10.1017/jfm.2013.412>
- 840 Lazar, A., Stegner, A., & Heifetz, E. (2013b). Inertial instability of intense stratified
841 anticyclones. Part 1. Generalized stability criterion. *Journal of Fluid Mechanics*, *732*, 457–484.
842 <https://doi.org/10.1017/jfm.2013.412>
- 843 Le Vu, B., A. Stegner, and T. Arsouze, 2018: Angular Momentum Eddy Detection and Tracking
844 Algorithm (AMEDA) and Its Application to Coastal Eddy Formation. *J. Atmos. Oceanic
845 Technol.*, **35**, 739–762, <https://doi.org/10.1175/JTECH-D-17-0010.1>
- 846 L'Hégaret, P., Carton, X., Louazel, S., & Boutin, G. (2016). Mesoscale eddies and submesoscale
847 structures of Persian Gulf Water off the Omani coast in spring 2011. *Ocean Sci.*, *12*(3), 687–701.
848 <https://doi.org/10.5194/os-12-687-2016>
- 849 Li, Q.-Y., Sun, L., & Lin, S.-F. (2016). GEM: a dynamic tracking model for mesoscale eddies in
850 the ocean. *Ocean Sci.*, *12*(6), 1249–1267. <https://doi.org/10.5194/os-12-1249-2016>
- 851 Lilly, J. M., & Gascard, J.-C. (2006). Wavelet ridge diagnosis of time-varying elliptical signals
852 with application to an oceanic eddy. *Nonlin. Processes Geophys.*, *13*(5), 467–483.
853 <https://doi.org/10.5194/npg-13-467-2006>
- 854 Mahadevan, A., Thomas, L. N., & Tandon, A. (2008). Comment on ‘Eddy/Wind Interactions
855 Stimulate Extraordinary Mid-Ocean Plankton Blooms’. *Science*, *320*(5875), 448–448.
856 <https://doi.org/10.1126/science.1152111>
- 857 McGillicuddy, D. J., Anderson, L. A., Bates, N. R., Bibby, T., Buesseler, K. O., Carlson, C. A.,
858 ... Steinberg, D. K. (2007). Eddy/Wind Interactions Stimulate Extraordinary Mid-Ocean
859 Plankton Blooms. *Science*, *316*(5827), 1021–1026. <https://doi.org/10.1126/science.1136256>

- 860 McGillicuddy, D.J., 2016. Mechanisms of Physical-Biological-Biogeochemical Interaction at the
861 Oceanic Mesoscale. *Annu. Rev. Mar. Sci.* 8, 125–159. [https://doi.org/10.1146/annurev-marine-](https://doi.org/10.1146/annurev-marine-010814-015606)
862 [010814-015606](https://doi.org/10.1146/annurev-marine-010814-015606)
- 863 Mewilliams, J.C., 2013. The Nature and Consequences of Oceanic Eddies, in: *Ocean Modeling*
864 in an Eddy Regime. American Geophysical Union (AGU), pp. 5–15.
865 <https://doi.org/10.1029/177GM03>
- 866 Meunier, T., Ménesguen, C., Schopp, R., & Le Gentil, S. (2014). Tracer Stirring around a
867 Meddy: The Formation of Layering. *Journal of Physical Oceanography*, 45(2), 407–423.
868 <https://doi.org/10.1175/JPO-D-14-0061.1>
- 869 Millot, C., Taupierletage, I., & Benzohra, M. (1990). The Algerian Eddies. *Earth-Science*
870 *Reviews*, 27(3), 203–219. [https://doi.org/10.1016/0012-8252\(90\)90003-E](https://doi.org/10.1016/0012-8252(90)90003-E)
- 871 Millot, C., 1999. Circulation in the Western Mediterranean Sea. *Journal of Marine Systems* 20, 423–
872 442. [https://doi.org/10.1016/S0924-7963\(98\)00078-5](https://doi.org/10.1016/S0924-7963(98)00078-5)
- 873 Mkhini, N., Coimbra, A. L. S., Stegner, A., Arsouze, T., Taupier-Letage, I., & Béranger, K.
874 (2014). Long-lived mesoscale eddies in the eastern Mediterranean Sea: Analysis of 20 years of
875 AVISO geostrophic velocities. *Journal of Geophysical Research: Oceans*, 119(12), 8603–8626.
876 <https://doi.org/10.1002/2014JC010176>
- 877 Nof, D., & Dewar, W. K. (1994). Alignment of lenses: laboratory and numerical experiments.
878 *Deep Sea Research Part I: Oceanographic Research Papers*, 41(8), 1207–1229.
879 [https://doi.org/10.1016/0967-0637\(94\)90041-8](https://doi.org/10.1016/0967-0637(94)90041-8)
- 880 Paillet, J., Le Cann, B., Carton, X., Morel, Y., & Serpette, A. (2002). Dynamics and Evolution of
881 a Northern Meddy. *Journal of Physical Oceanography*, 32(1), 55–79.
882 [https://doi.org/10.1175/1520-0485\(2002\)032<0055:DAEOAN>2.0.CO;2](https://doi.org/10.1175/1520-0485(2002)032<0055:DAEOAN>2.0.CO;2)
- 883 Pascual, A., Pujol, M.-I., Larnicol, G., Le Traon, P.-Y., & Rio, M.-H. (2007). Mesoscale
884 mapping capabilities of multisatellite altimeter missions: First results with real data in the
885 Mediterranean Sea. *Journal of Marine Systems*, 65(1), 190–211.
886 <https://doi.org/10.1016/j.jmarsys.2004.12.004>
- 887 Perez, J. D. S. (2003). Evolution of the open-sea eddy ALGERS'98 in the Algerian Basin with
888 Lagrangian trajectories and remote sensing observations. *Journal of Marine Systems*, 43(3–4),
889 105–131. <https://doi.org/10.1016/j.jmarsys.2003.08.001>
- 890 Pietri, A., Karstensen, J., 2018. Dynamical Characterization of a Low Oxygen Submesoscale
891 Coherent Vortex in the Eastern North Atlantic Ocean. *Journal of Geophysical Research: Oceans*
892 123, 2049–2065. <https://doi.org/10.1002/2017JC013177>
- 893 Pinot, J.-M., & Ganachaud, A. (1999). The role of winter intermediate waters in the spring-
894 summer circulation of the Balearic Sea: 1. Hydrography and inverse box modeling. *Journal of*
895 *Geophysical Research: Oceans*, 104(C12), 29843–29864. <https://doi.org/10.1029/1999JC900202>
- 896 Puillat, I., Taupier-Letage, I., & Millot, C. (2002). Algerian Eddies lifetime can near 3 years.
897 *Journal of Marine Systems*, 31(4), 245–259. [https://doi.org/10.1016/S0924-7963\(01\)00056-2](https://doi.org/10.1016/S0924-7963(01)00056-2)

- 898 Pujol, M.-I., Faugère, Y., Taburet, G., Dupuy, S., Pelloquin, C., Ablain, M., & Picot, N. (2016).
899 DUACS DT2014: the new multi-mission altimeter data set reprocessed over 20 years. *Ocean*
900 *Sci.*, *12*(5), 1067–1090. <https://doi.org/10.5194/os-12-1067-2016>
- 901 Rio, M.-H., Poulain, P.-M., Pascual, A., Mauri, E., Larnicol, G., & Santoleri, R. (2007). A Mean
902 Dynamic Topography of the Mediterranean Sea computed from altimetric data, in-situ
903 measurements and a general circulation model. *Journal of Marine Systems*, *65*(1), 484–508.
904 <https://doi.org/10.1016/j.jmarsys.2005.02.006>
- 905 Robinson, A. R. (1983). *Eddies in Marine Science* (609 pp.). Berlin: Springer Verlag.
906 <https://doi.org/10.1007/978-3-642-69003-7>
- 907 Ruiz, S., Font, J., Emelianov, M., Isern-Fontanet, J., Millot, C., Salas, J., & Taupier-Letage, I.
908 (2002). Deep structure of an open sea eddy in the Algerian Basin. *Journal of Marine Systems*,
909 *33–34*, 179–195. [https://doi.org/10.1016/S0924-7963\(02\)00058-1](https://doi.org/10.1016/S0924-7963(02)00058-1)
- 910 Ruiz, S., Pascual, A., Garau, B., Pujol, I., & Tintoré, J. (2009). Vertical motion in the upper
911 ocean from glider and altimetry data. *Geophysical Research Letters*, *36*(14), L14607.
912 <https://doi.org/10.1029/2009GL038569>
- 913 Salas J., 2003. Evolution of the open-sea eddy ALGERS'98 in the Algerian Basin with
914 Lagrangian trajectories and remote sensing observations. *Journal of Marine Systems* *43*, 105–
915 131. <https://doi.org/10.1016/j.jmarsys.2003.08.001>
- 916 Testor, P., Send, U., Gascard, J.-C., Millot, C., Taupier-Letage, I., & Béranger, K. (2005). The
917 mean circulation of the southwestern Mediterranean Sea: Algerian Gyres. *Journal of*
918 *Geophysical Research: Oceans*, *110*(C11), C11017. <https://doi.org/10.1029/2004JC002861>
- 919 Taupier-Letage, I., Puillat, I., Millot, C., Raimbault, P., 2003. Biological response to mesoscale
920 eddies in the Algerian Basin. *Journal of Geophysical Research: Oceans* *108*.
921 <https://doi.org/10.1029/1999JC000117>
- 922 Vargas-Yáñez, M., Zunino, P., Schroeder, K., López-Jurado, J. L., Plaza, F., Serra, M., ... Salat,
923 J. (2012). Extreme Western Intermediate Water formation in winter 2010. *Journal of Marine*
924 *Systems*, *105–108*, 52–59. <https://doi.org/10.1016/j.jmarsys.2012.05.010>
- 925 Yi, J., Du, Y., He, Z., & Zhou, C. (2014). Enhancing the accuracy of automatic eddy detection
926 and the capability of recognizing the multi-core structures from maps of sea level anomaly.
927 *Ocean Sci.*, *10*(1), 39–48. <https://doi.org/10.5194/os-10-39-2014>
- 928 Zhong, Y., Bracco, A., Tian, J., Dong, J., Zhao, W., & Zhang, Z. (2017). Observed and simulated
929 submesoscale vertical pump of an anticyclonic eddy in the South China Sea. *Scientific Reports*,
930 *7*. <https://doi.org/10.1038/srep44011>

figure 1.

sea surface temperature

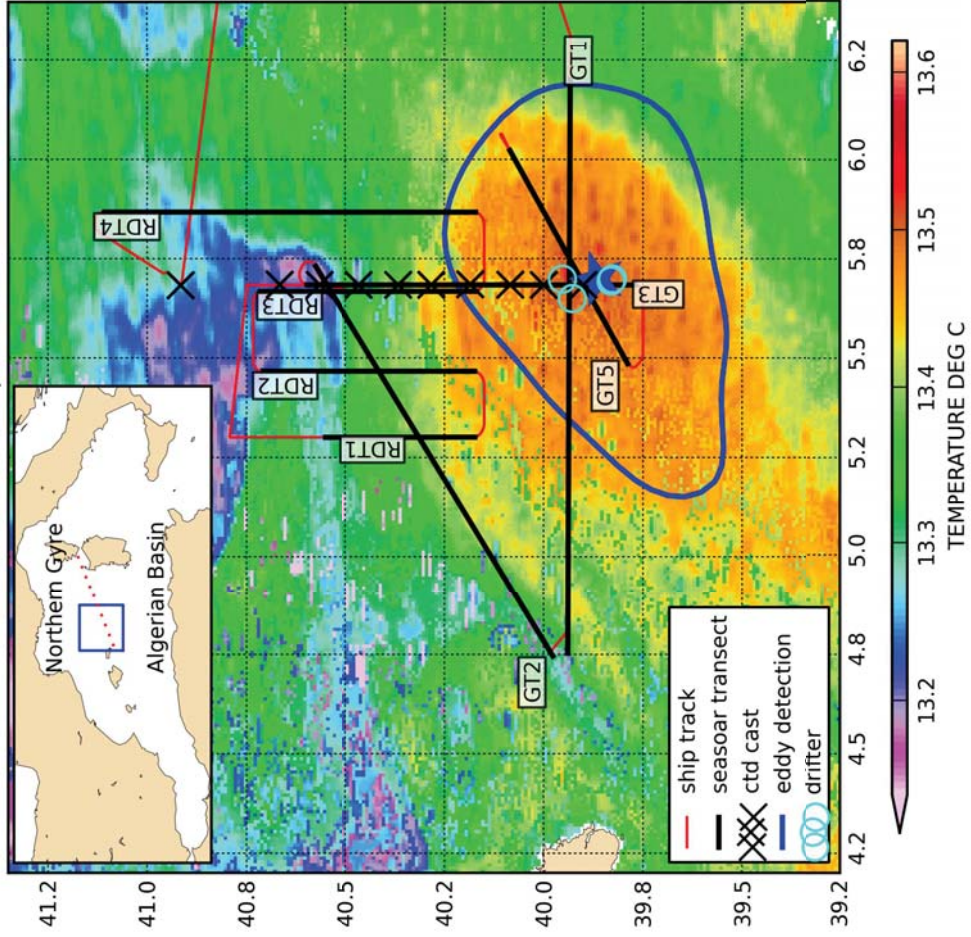


figure 2.

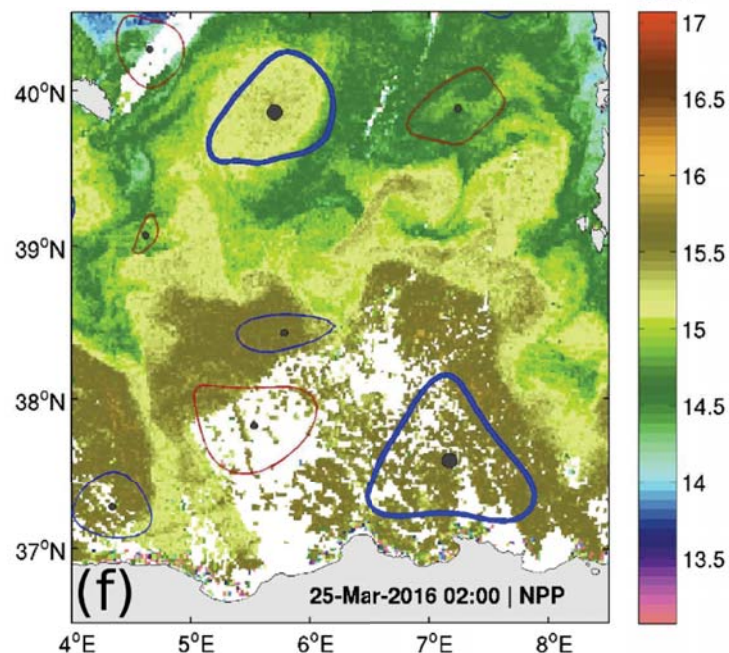
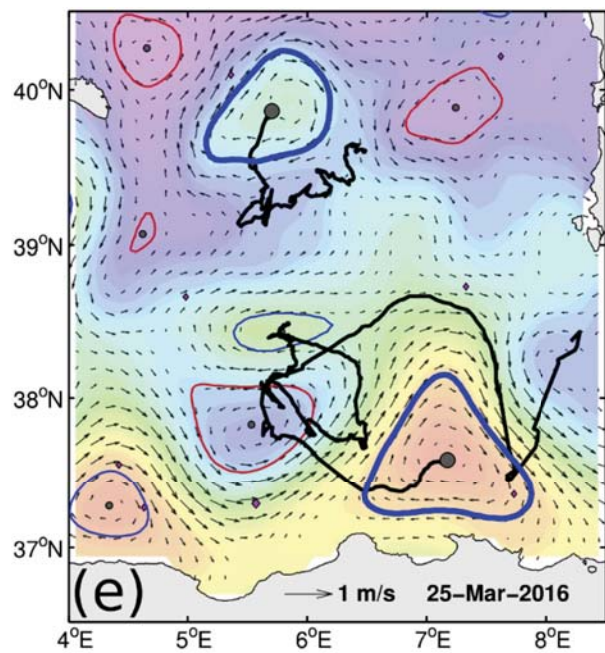
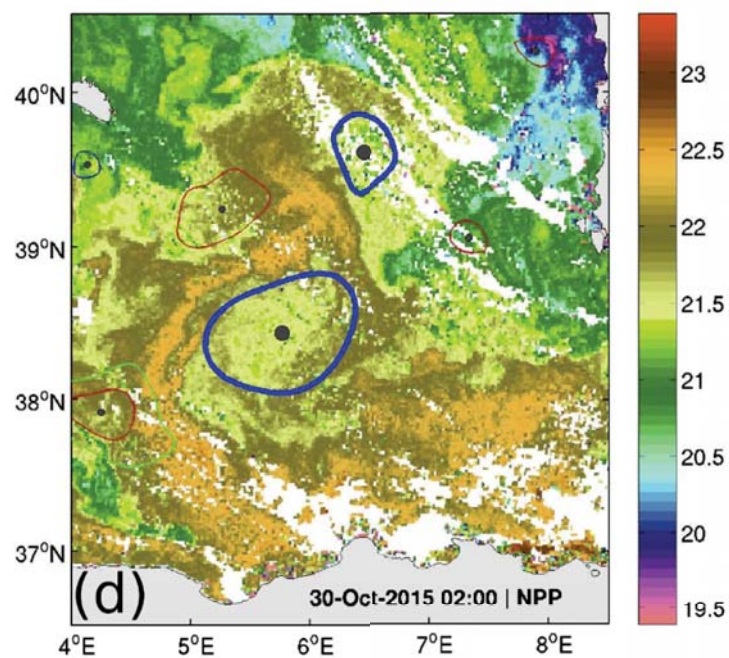
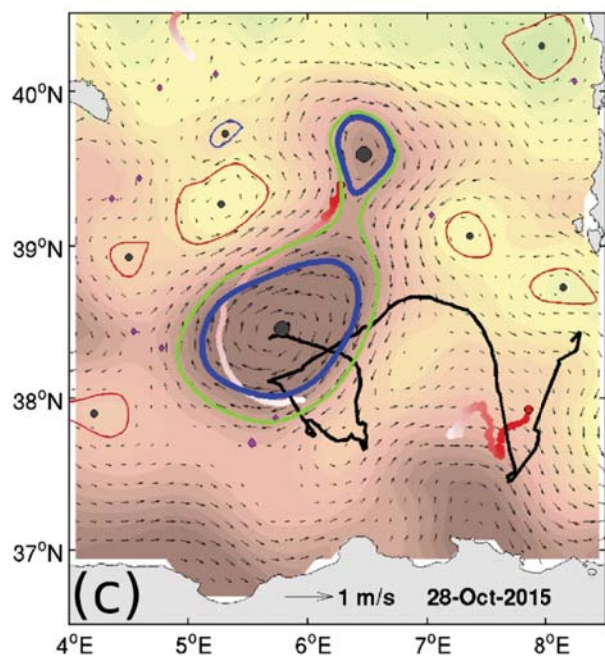
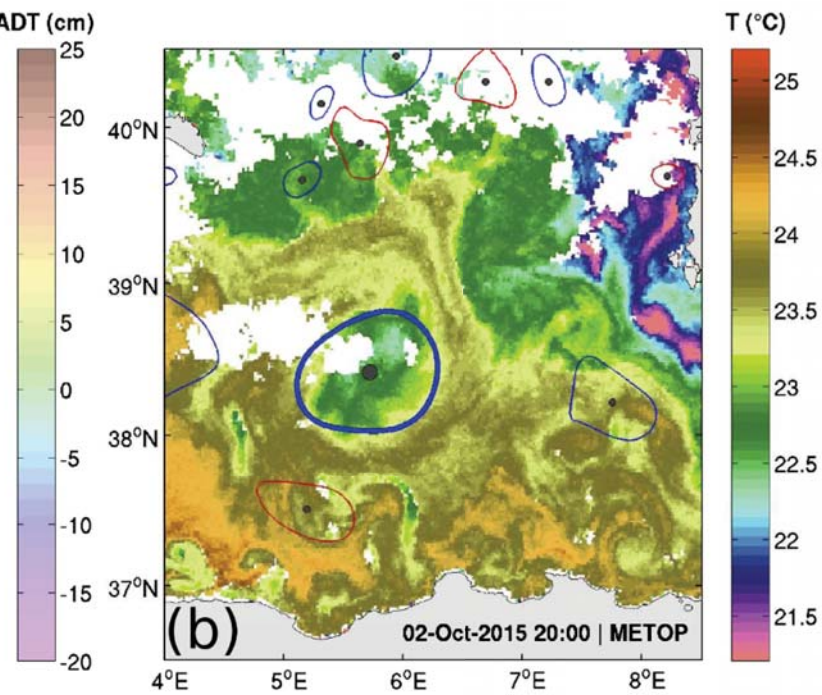
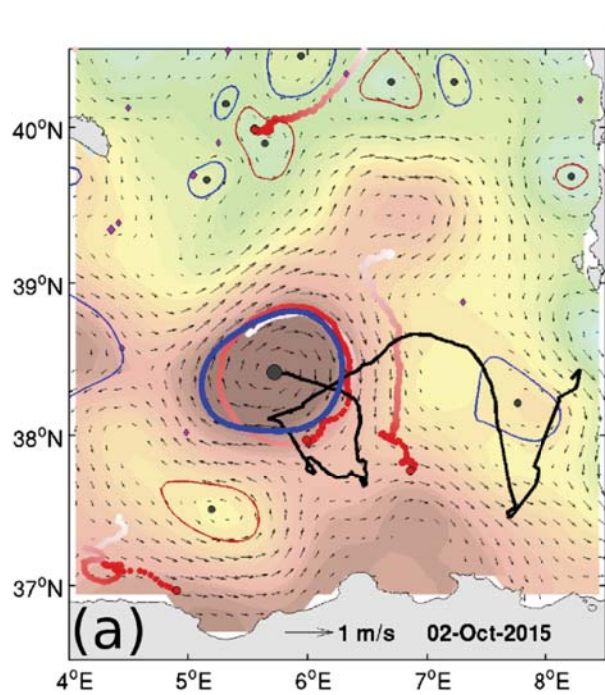


figure 3.

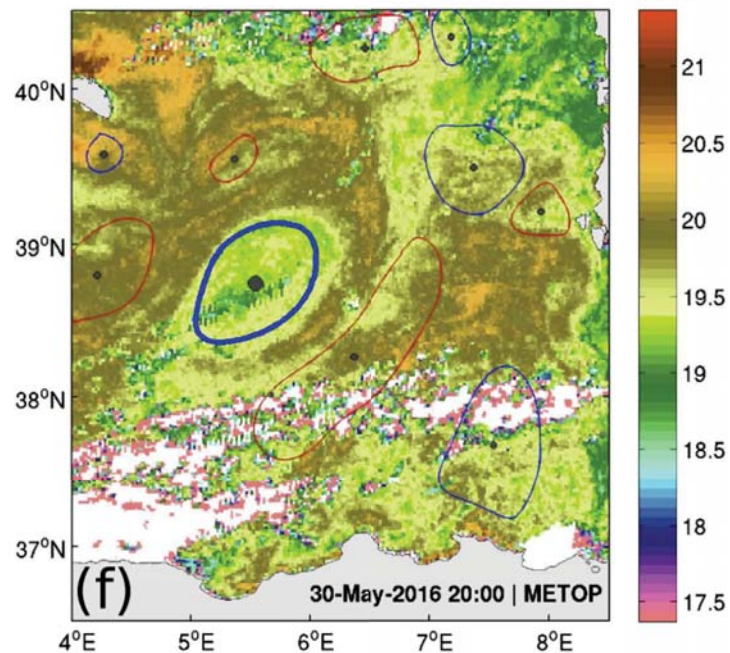
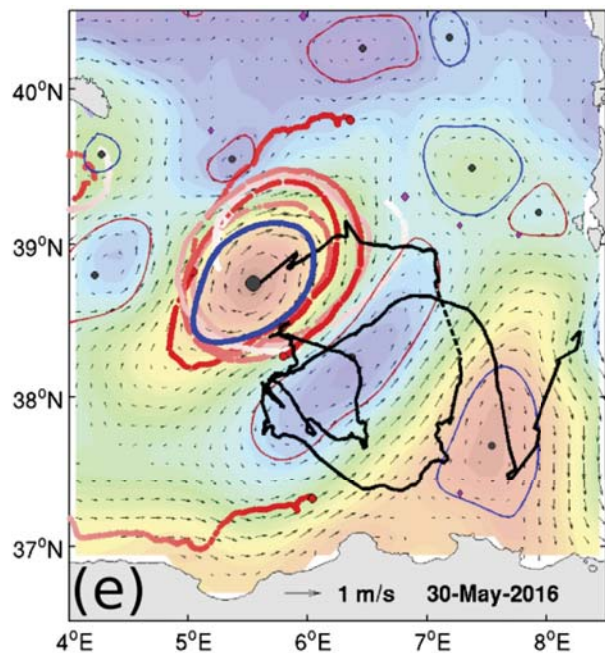
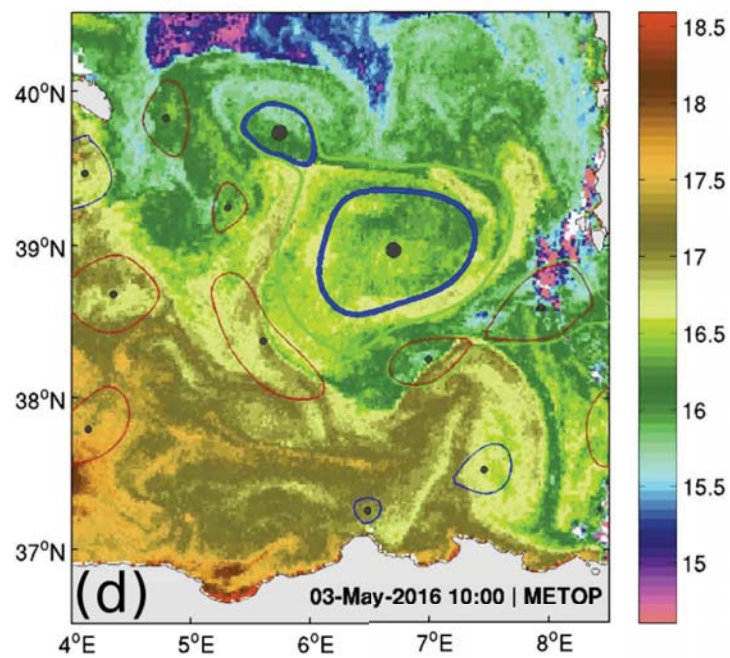
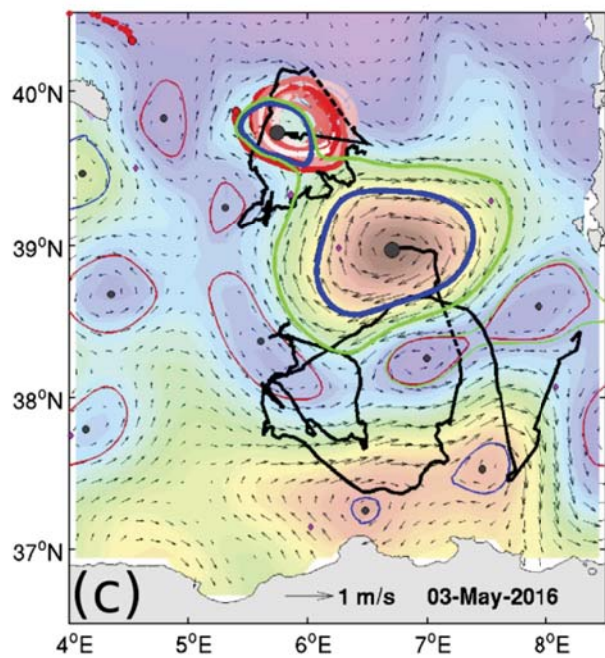
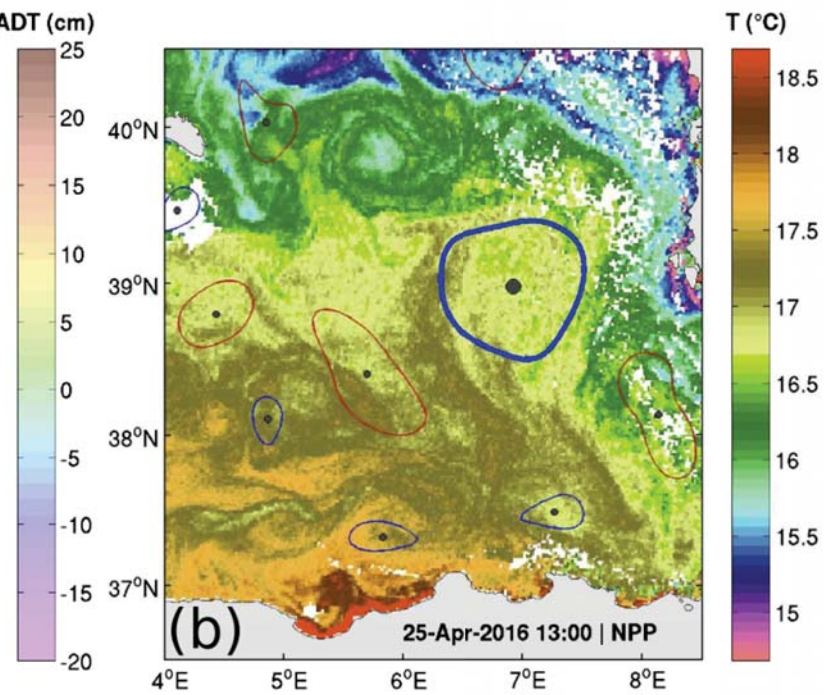
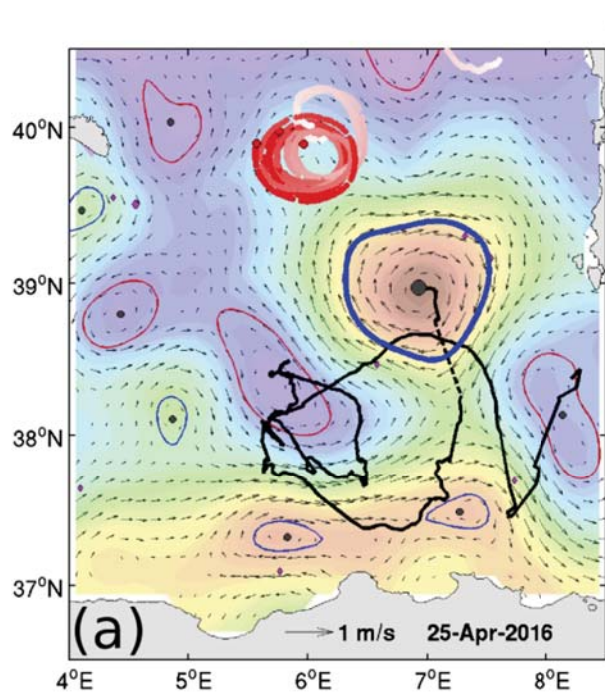


figure 4.

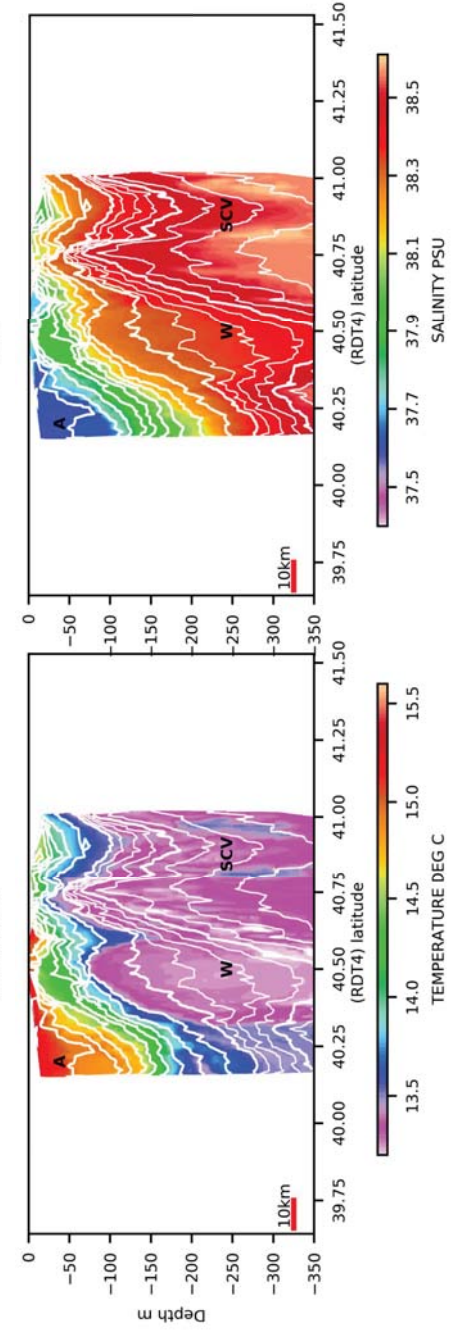
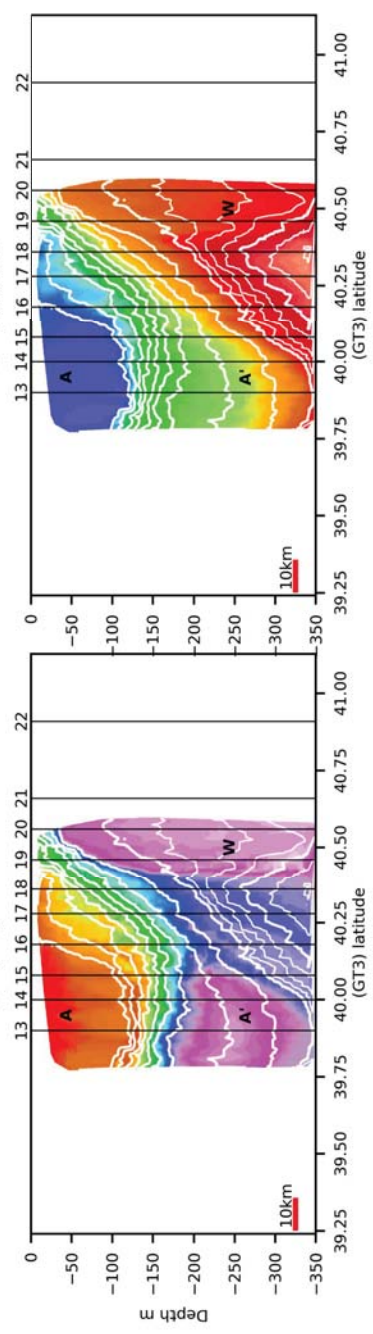
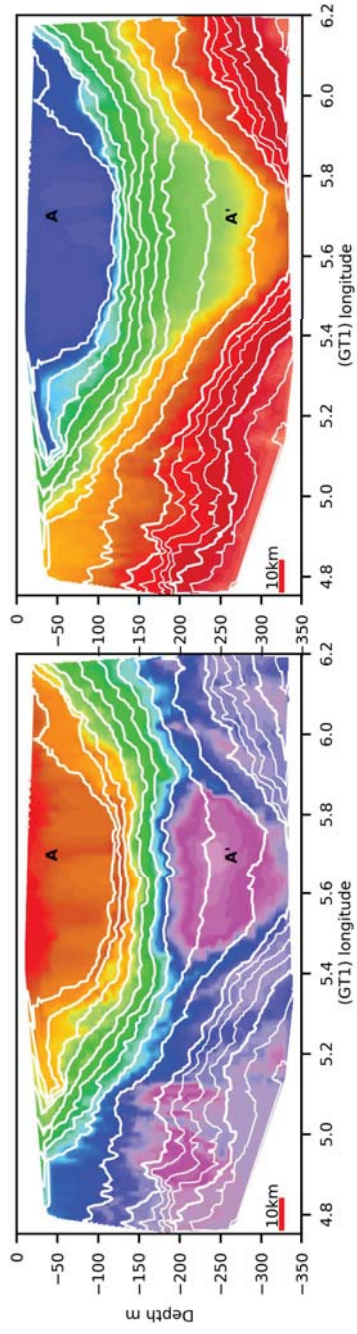


figure 5.

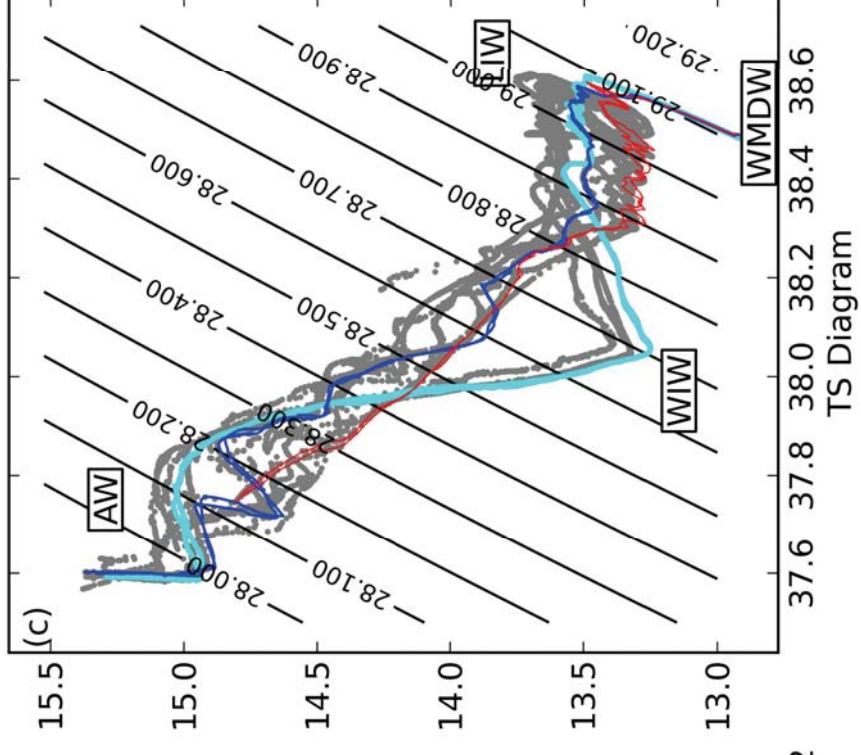
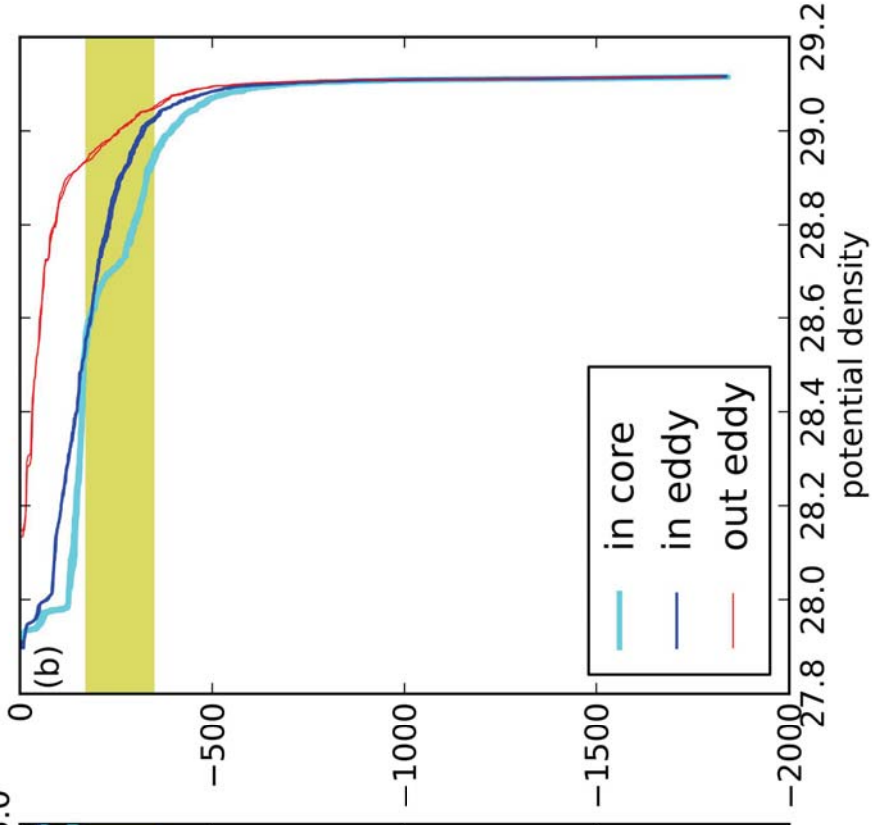
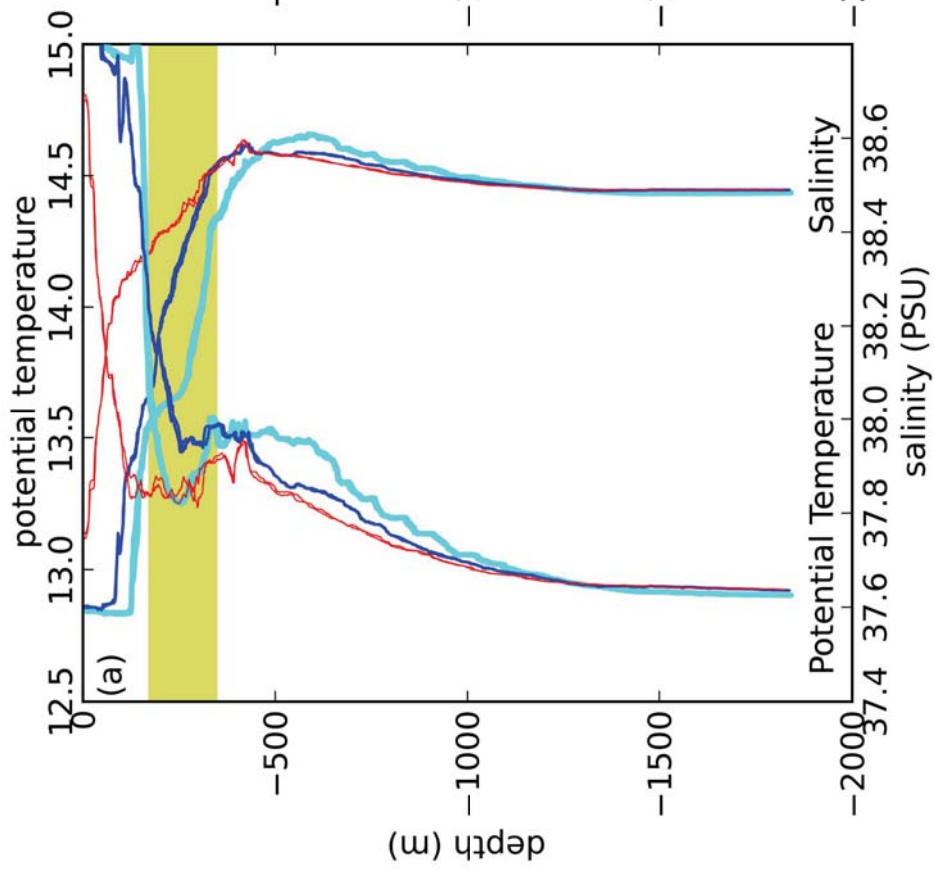


figure 6.

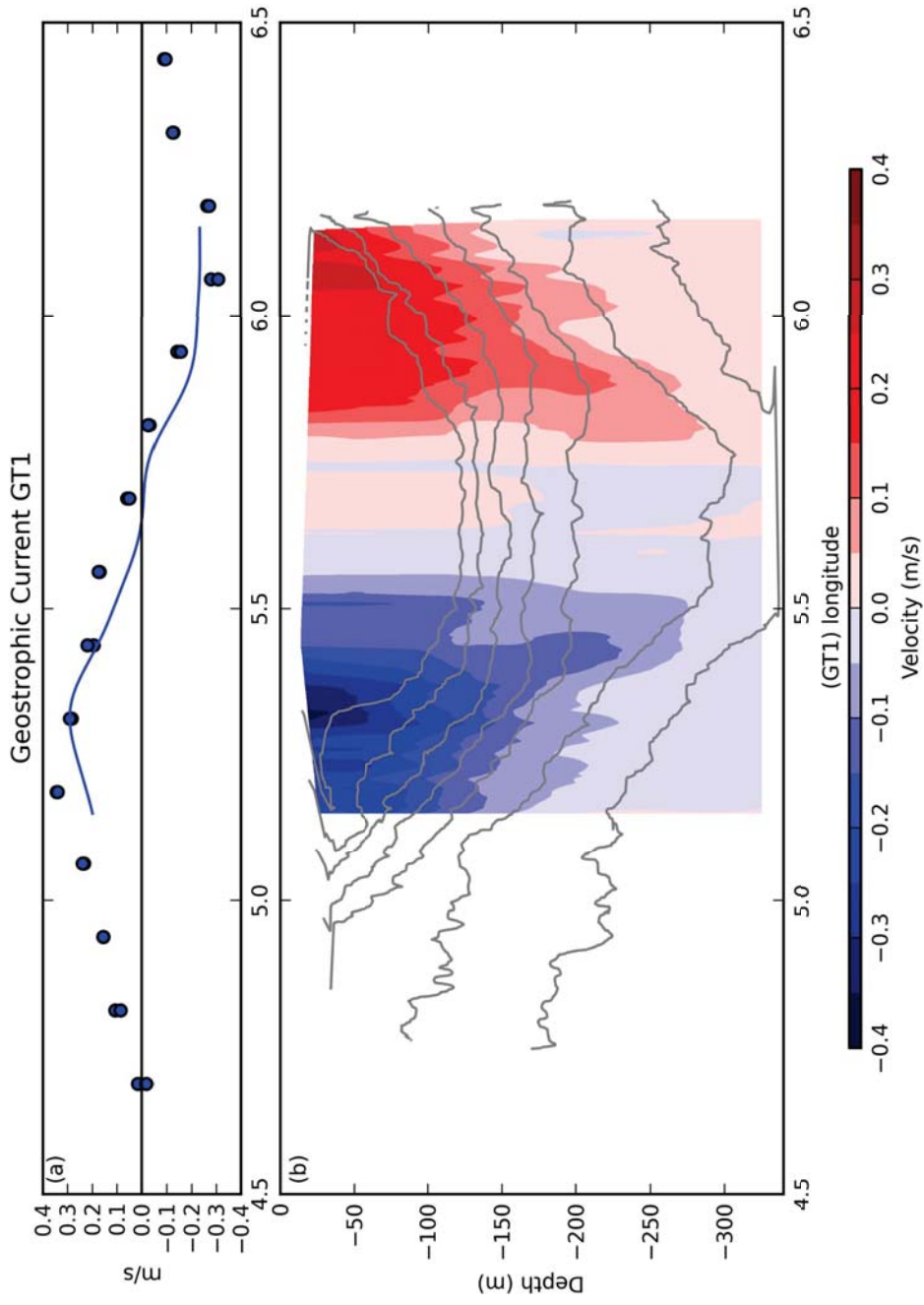
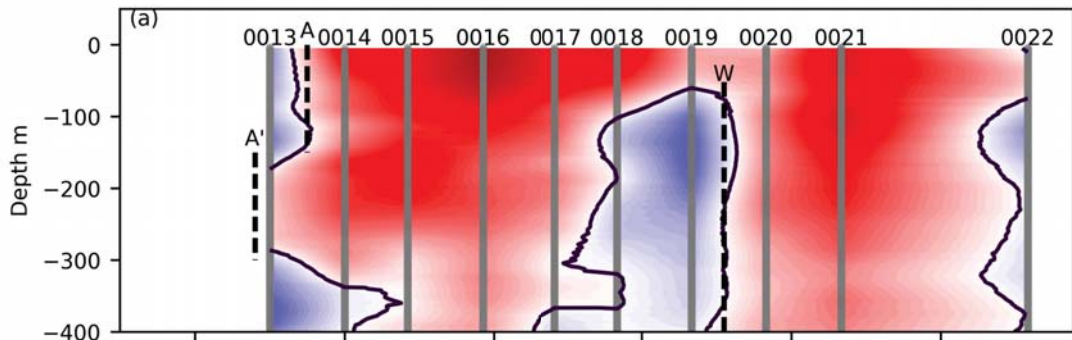


figure 7.

Zonal Current from LADCP Transect GT3



Geostrophic Current from Seasoar Transect GT3 (depth_ref = 360)

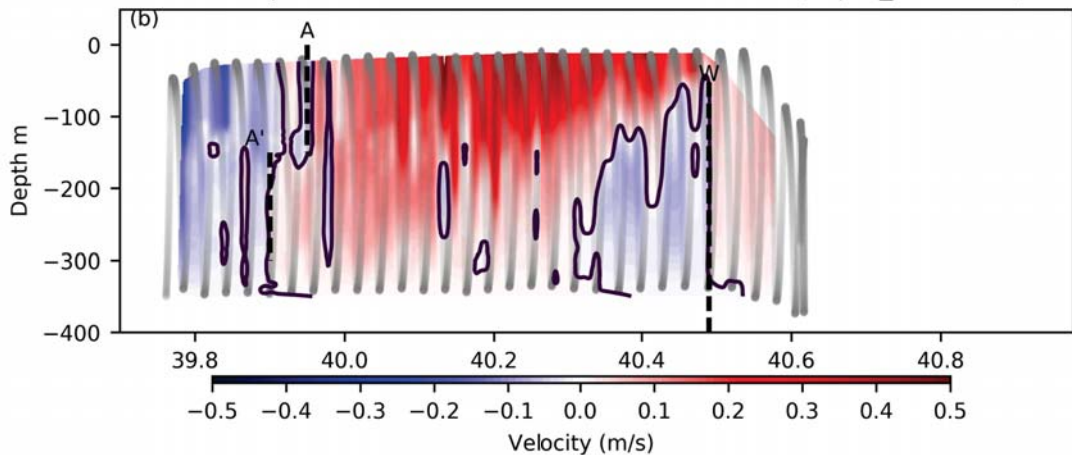


figure 8.

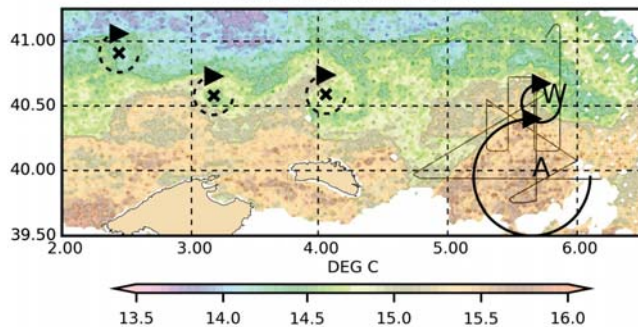
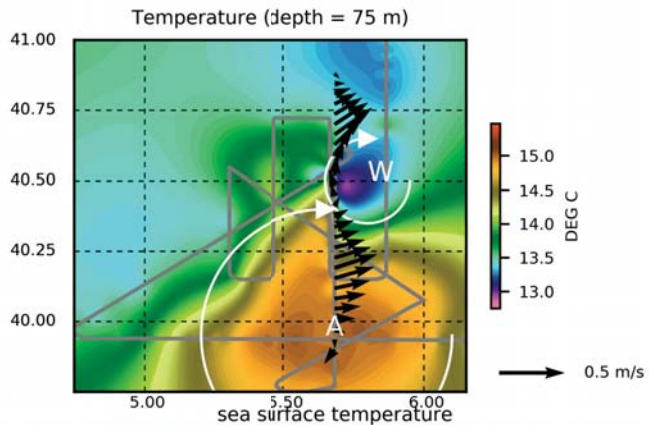


figure 9.

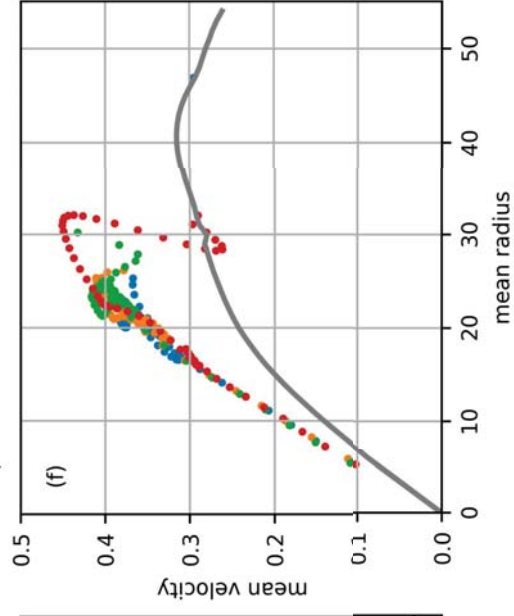
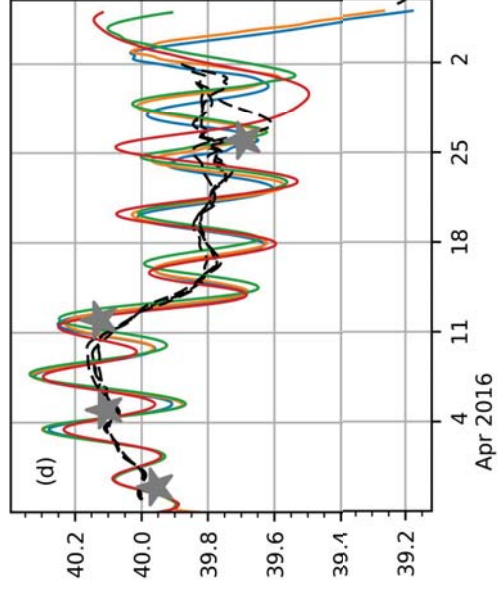
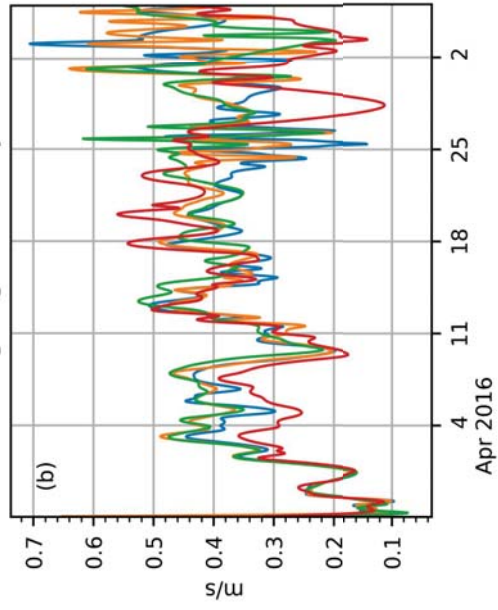
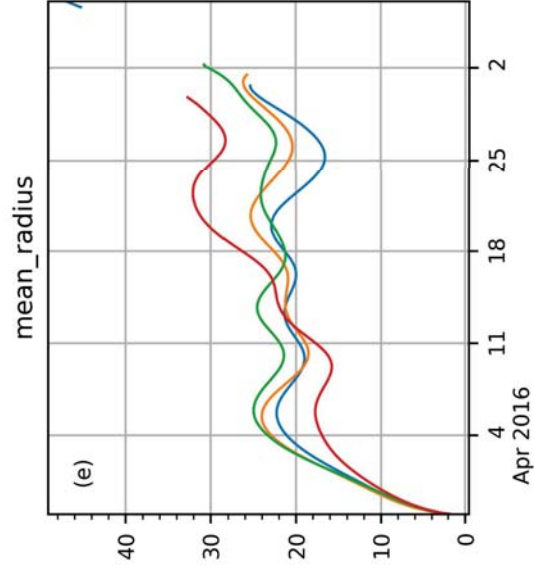
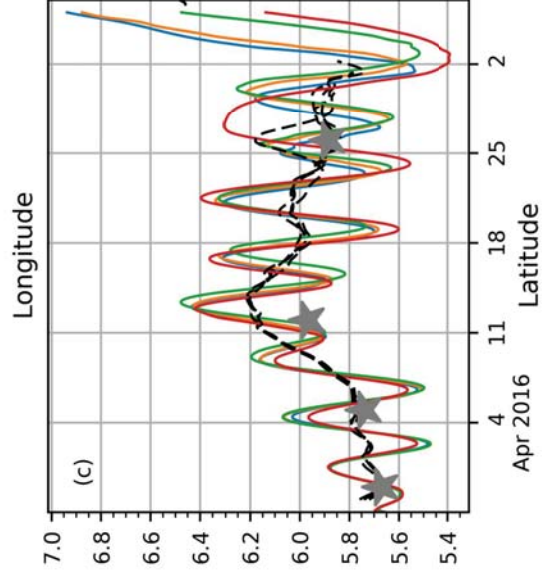
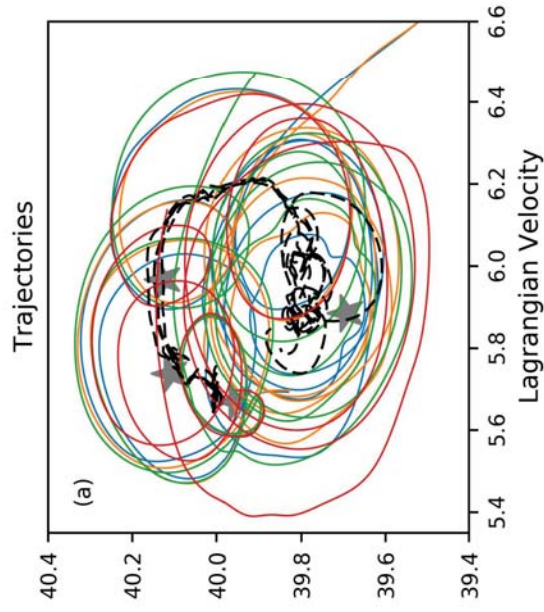


figure 10.

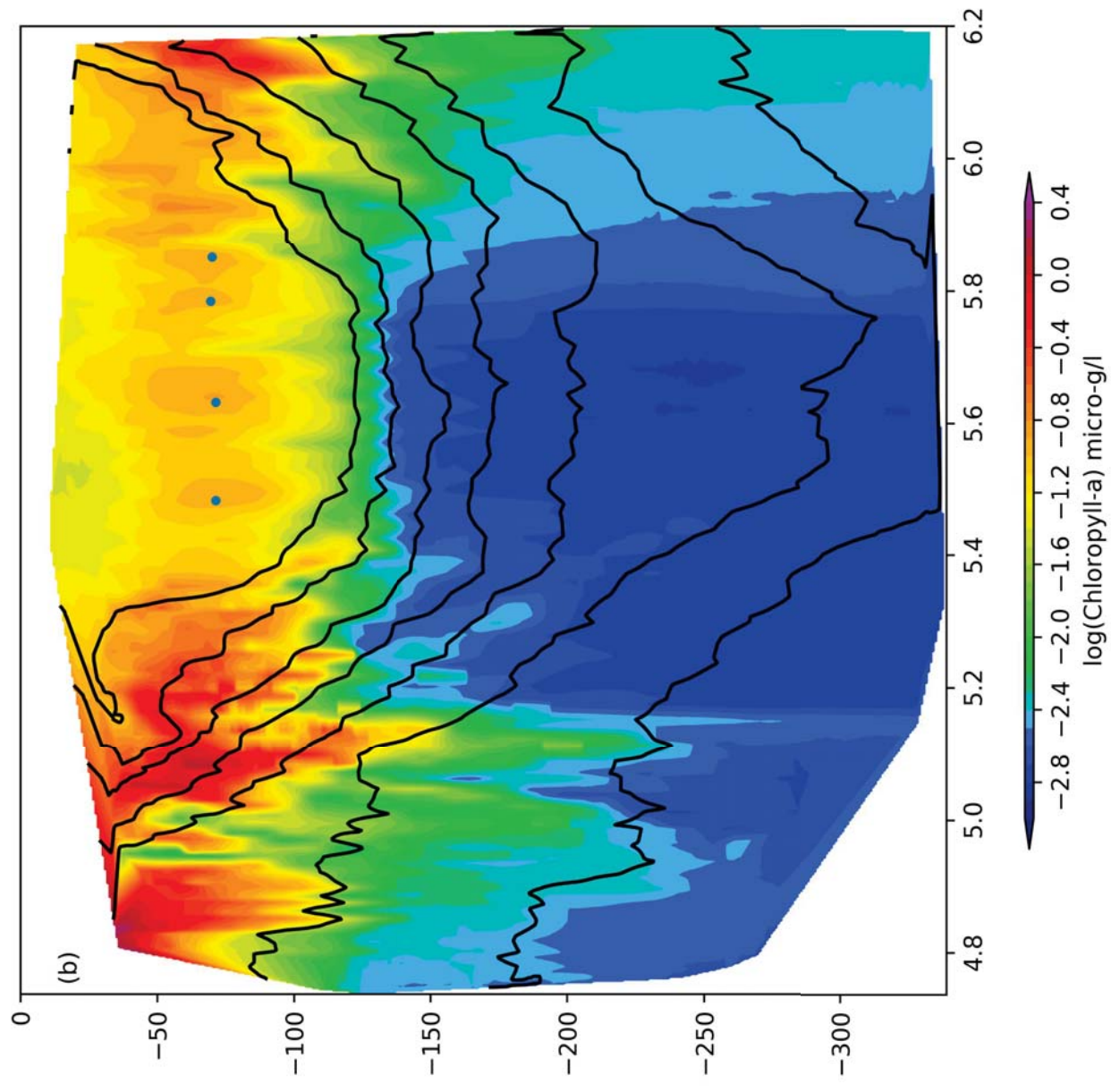
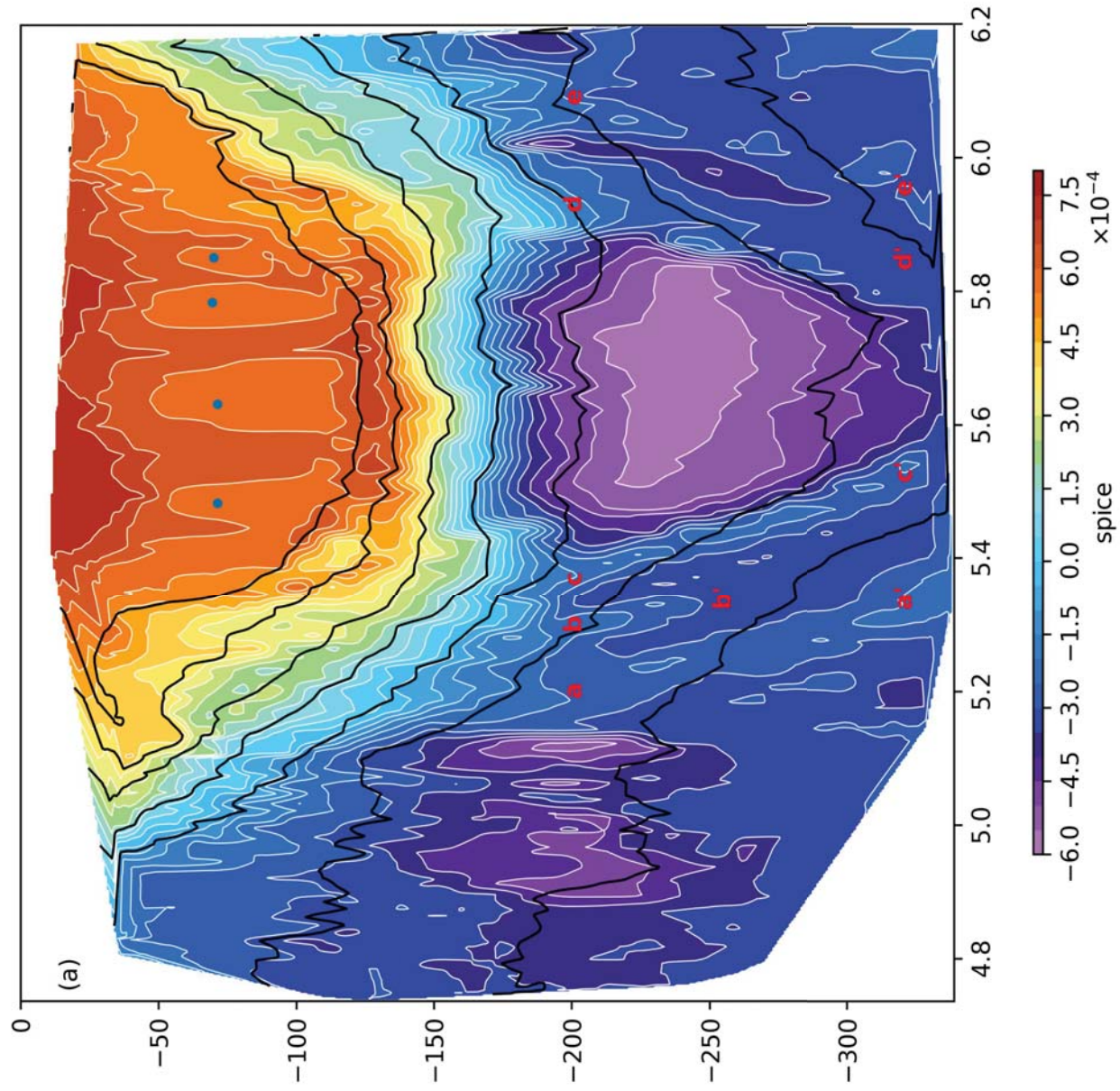


figure 11.

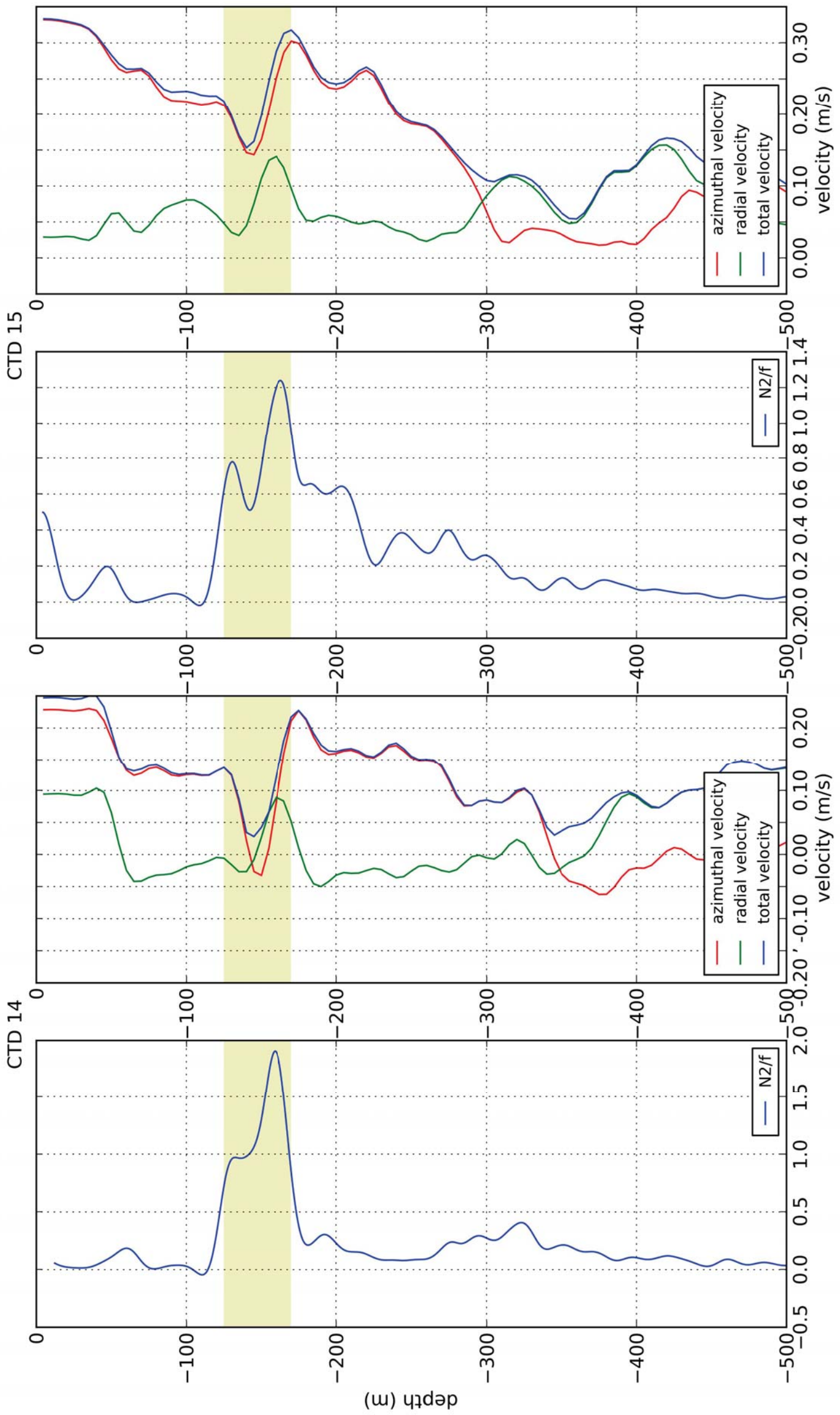


figure 12.

